https://doi.org/10.5194/egusphere-2025-6272
Preprint. Discussion started: 31 December 2025

Near real-time inversion of high-resolution anthropogenic carbon emissions in the Pearl River Delta region based on the four-dimensional local ensemble transform Kalman filter

Yike Wag[1], Yueming Cheng[2], Boru Mai[1], Tie Dai[2], Xuejiao Deng[1], Tao Deng[1], Xiaoli Zhao[3],Yiwei Diao[4], Feng Xia[1], Miao Liang[5], Ying Li[6], Yixiao Zhu[1]

[1]Institute of Tropical and Marine Meteorology, China Meteorological Administration (CMA), Guangzhou, China
[2]State Key Laboratory of Numerical Modeling for Atmospheric Sciences and Geophysical Fluid Dynamics, Institute of Atmospheric Physics, Chinese Academy of Sciences, Beijing, China
[3]Observation and Network Department, Guangdong Meteorological Bureau, Guangzhou, China
[4]Wuxi University, Wuxi, China
[5]Meteorological Observation Center, China Meteorological Administration, Beijing, China
[6]Department of Ocean Science and Engineering, Southern University of Science and Technology, Shenzhen, China

Correspondence: Boru Mai (mbr4@163.com), Tie Dai (daitie@mail.iap.ac.cn)

Abstract. For climate mitigation, it is necessary to address the challenges of the dynamic updating and quantitative assessment of anthropogenic CO_2 emissions at meso-to-microscales. This study developed a kilometer-scale carbon assimilation system (the Guangzhou Regional Atmospheric Composition and Environment Forecasting System–Greenhouse Gas–Data Assimilation, GRACES-GHG-DA) by coupling the weather research and forecasting–greenhouse gas (WRF-GHG) model with the four-dimensional local ensemble transform Kalman filter (4D-LETKF). GRACES-GHG-DA constructs a near-real-time 4-km anthropogenic emission inventory, constrained by simulated CO_2 observation data from seven high-precision greenhouse gas monitoring stations in the Pearl River Delta (PRD) region, to analyze spatiotemporal emission distributions and their relationship with ambient CO_2 concentrations. The results indicate that: (1) GRACES-GHG-DA accurately downscales CO_2 concentrations from a resolution of 36 to 4 km, with the finer resolution better capturing meso- and micro-scale variations (hourly and monthly mean biases of −0.77 and −0.51 ppm, respectively). (2) In 2022, the inverted annual anthropogenic CO_2 flux in core PRD areas exceeded 7500 g C m^{-2} a^{-1}, contrasting with values below 1000 g C m^{-2} a^{-1} in peripheral regions. Compared to the inversion estimates, statistical inventories (EDGAR, ODIAC, GCP, and MEIC) underestimated total emissions by 14.71% on average. (3) Seasonal anthropogenic emissions were 24.03, 29.86, 30.61, and 27.26 Tg C for spring, summer, autumn, and winter, respectively, showing a unimodal diurnal pattern largely influenced by fossil-fuel electricity generation.(4) Anthropogenic emissions are not the dominant factor governing atmospheric CO_2 concentrations in the PRD; vegetation carbon uptake/release, boundary layer evolution, and regional transport also play critical roles.

1 Introduction

Currently, two primary approaches are employed to estimate atmospheric CO_2 emissions. The first is the "bottom-up" method, which relies on emission inventories, while the second is the "top-down" method, which integrates multi-platform observations with atmospheric transport and inversion models (Masarie et al., 1995; Gloor et al., 2000). Owing to limited

https://doi.org/10.5194/egusphere-2025-6272
Preprint. Discussion started: 31 December 2025

greenhouse gas monitoring sites and insufficient high-precision observational data, the bottom-up method remains the most widely used technique for CO_2 emission estimation. However, CO_2 emission inventories carry substantial uncertainties, including uncertainties introduced by statistical data, emission factors, and spatiotemporal allocation schemes. The discrepancies among different CO_2 emission inventories range from 70% to 300% (Han et al., 2020), and it is difficult to identify or locate unknown emission sources utilizing the bottom-up approach (Cai et al., 2021).

At the 49th Session of the Intergovernmental Panel on Climate Change (IPCC) in 2019, a revised scheme for the 2006 IPCC Guidelines for National Greenhouse Gas Inventories was adopted (IPCC, 2019). This scheme introduced a new technique for emission inventory validation: using greenhouse gas fluxes from the top-down inversion of atmospheric concentration data to verify bottom-up emission inventories. The goal of this method is to accurately capture regional variations in greenhouse gas concentrations and their emission and absorption dynamics.

To address limitations in numerical inversion and assimilation for the investigation of greenhouse gas sources and sinks, researchers have integrated atmospheric CO_2 concentration measurements with meteorological data and atmospheric chemical transport models—including Goddard Earth Observing System-Chem (GEOS-Chem), The Global Atmospheric Tracer Model 5 (TM5), the Model for Ozone and Related Chemical Tracers Version 4 (MOZART-4), and the Laboratoire de Météorologie Dynamique Zoom (LMDZ)—to estimate regional carbon fluxes and concentrations via data assimilation (Tian et al., 2013; Peng et al., 2015; Thompson et al., 2016; Monteil et al., 2020; Jiang et al., 2021).

The CarbonTracker (CT) global carbon flux inversion system, developed by the National Oceanic and Atmospheric Administration (NOAA), is a pioneering framework for estimating carbon uptake and emissions (Peters et al., 2007). Driven by the TM5 atmospheric transport model, the CT system employs an ensemble Kalman filter (EnKF) to assimilate observed CO_2 concentrations. The terrestrial ecosystem carbon fluxes are calculated online using the Carnegie–Ames–Stanford approach (CASA) model. Additionally, CT has been operating continuously and has expanded to regional applications, including Europe (e.g., CT-Europe; Peter et al., 2010; Peylin et al., 2013) and Asia (e.g., CT-Asia; Cheng et al., 2013; Zhang, 2014a, 2014b).

The global Carbon Cycle Data Assimilation System (CCDAS) is an additional crucial framework (Rayner et al., 2005). The CCDAS further integrates global station data, including terrestrial ecosystem carbon fluxes, remote sensing-derived surface parameters, and CO_2 concentrations, to optimize ecosystem model parameters and assimilate carbon fluxes. This integration has enabled the development of global carbon cycle reanalysis datasets (Kaminski et al., 2013; Schürmann et al., 2016; Scholze et al., 2019).

In recent years, Chinese scientists have made significant contributions to the advancement of global carbon data assimilation systems (Chen & Zhang, 2015; Chen et al., 2015) and developed several assimilation systems, including the

https://doi.org/10.5194/egusphere-2025-6272
Preprint. Discussion started: 31 December 2025

Global Carbon Assimilation System (GCAS) (Zhang et al., 2014; Ju et al., 2019) and Tan-Tracker (Tian et al., 2014; Han & Tian, 2019).

Due to limitations in spatiotemporal resolution, global models fail to accurately capture how meso- and micro-scale meteorological processes such as wind fields, topography, and land–atmosphere exchange fluxes influence the spatiotemporal distribution of CO_2. This leads to significant errors when applying these models to high-resolution regional carbon source–sink inversion. Compared with coarse-resolution global models, mesoscale chemical transport models explicitly resolve processes such as anthropogenic CO_2 emissions, vegetation carbon uptake, boundary-layer turbulence, and atmospheric transport. This reduces the impact of model uncertainty on regional carbon assimilation systems.

At the regional to urban scale, mesoscale atmospheric chemical transport models are commonly utilized as a driving framework in combination with techniques such as Kalman filtering and variational assimilation to perform high-resolution carbon assimilation and inversion. For example, Kou et al. (2023) employed the community multiscale air quality (CMAQ) mesoscale model to conduct EnKF-based carbon satellite assimilation. This study inverted China's carbon source–sink distribution and provided top-down results for provincial-scale terrestrial carbon sinks. Guo et al. developed a multi-level nested grid system for carbon monitoring, assimilation, inversion, and accounting, designated as the China carbon monitoring and verification support at the regional level (CCMVS-R) system (Guo et al., 2023). This system integrates the coupled three-dimensional (3D) weather research and forecasting–greenhouse gas (WRF-GHG) model with the proper orthogonal decomposition–based four-dimensional (4D) ensemble variational assimilation technique (POD 4DVar). They employed this system to alter the carbon emission characteristics of Shanxi Province. Wu et al. (2016) employed the chemistry transport model (CHIMERE) coupled with a Bayesian model to perform the urban-scale assimilation and inversion of anthropogenic CO_2 sources in Paris while also providing urban carbon emission monitoring to support the monitoring, reporting, and verification (MRV) process.

In terms of temporal resolution, current regional-urban carbon assimilation inversions are primarily constrained to daily and weekly scales (Bréon et al., 2015; Wu et al., 2016). There are still critical challenges in dynamically updating and quantitatively accounting for meso- and micro-scale carbon sources and sinks. Recently, Peng et al. (2022) used the CMAQ model and ensemble square root filter (EnSRF) to develop an hourly carbon flux prediction operator that incorporates diurnal variations. They further applied a joint data assimilation system for CO_2 fluxes and concentrations (JDAS) to reduce uncertainties in carbon assimilation. However, this study primarily assimilated CO_2 observations from China's background regions and lacked representative nighttime observations and sufficient data to characterize urban CO_2 emissions (Kou et al., 2024).

Currently, China is participating in significant international efforts to reduce greenhouse gas emissions. In its 14th Five-Year Plan, the Chinese government established goals to reach peak CO_2 emissions before 2030 ("peak carbon") and

https://doi.org/10.5194/egusphere-2025-6272
Preprint. Discussion started: 31 December 2025

strive for carbon neutrality before 2060. To achieve these national "dual carbon" goals, challenges related to emissions reduction are likely to emerge across regions, provinces, and cities as the targets are implemented at the regional, provincial, and municipal levels. Thus, there is an urgent need to develop a kilometer-scale resolution CO_2 assimilation inversion technique for urban areas to address the dynamic updating and quantitative estimation of anthropogenic emissions and natural carbon sinks.

The 4D local ensemble transform Kalman filter (4D-LETKF) is a new data assimilation technique that has been developed in recent years. Compared to 3D assimilation techniques, 4D-LETKF has significant computational advantages in hourly data assimilation accuracy; and it can assimilate asynchronous observational data, thereby enhancing model analysis fields (Dai et al., 2019a). Studies suggest that 4D-LETKF has significant potential for the top-down dynamic inversion of atmospheric pollutant emissions (Dai et al., 2019b; Cheng et al., 2019; Dai et al., 2021). This study had three objectives: (1) to establish a high-resolution carbon source–sink data assimilation and inversion system by coupling the WRF-GHG model with 4D-LETKF; (2) to develop a 4-km-resolution anthropogenic emission inventory with hourly updates and compare/validate it against bottom-up statistical inventories; and (3) to characterize the spatiotemporal distribution of top-down anthropogenic CO_2 emissions and investigate their impacts on atmospheric CO_2 concentrations. The remainder of this paper is structured as follows: Section 2 outlines the model configuration and data sources. Section 3 presents the verification and analysis of inverted CO_2 concentrations across multiple spatiotemporal scales. Section 4 analyzes the spatial distribution of top-down anthropogenic CO_2 emissions in the Pearl River Delta (PRD) and compares these emissions with bottom-up inventories. Section 5 examines the temporal distribution of regional top-down anthropogenic CO_2 emission sources and their relationship with atmospheric CO_2 concentrations. The main conclusions are summarized in Section 6.

2 Model configuration and data sources

2.1 WRF-GHG modeling and calculation of the net ecosystem exchange (NEE)

The WRF-GHG is a weather–biosphere numerical model established through the direct and dynamic coupling of the weather research and forecasting (WRF) model with the vegetation photosynthesis and respiration model (VPRM). The WRF-GHG can directly simulate terrestrial ecosystem CO_2 fluxes, predict the spatiotemporal distribution and dynamic variations of atmospheric CO_2 concentrations, and quantify the contributions of different sources (e.g., biogenic, anthropogenic, and biomass burning) to total CO_2 concentrations. In the coupled model, the WRF model supplies online meteorological field data to drive the VPRM. The CO_2 fluxes simulated by the VPRM are then used to assess the spatiotemporal evolution of biospheric CO_2 fluxes and concentrations at regional meso- and micro-scales.

The VPRM is a diagnostic greenhouse gas model for terrestrial ecosystems. It utilizes satellite-derived parameters, including the land surface water index (LSWI) and the enhanced vegetation index (EVI). Combined with the 2-m air

https://doi.org/10.5194/egusphere-2025-6272
Preprint. Discussion started: 31 December 2025

temperature (T2) and downward shortwave radiation (SWDOWN) obtained via WRF simulations, the model estimates the NEE (Mahadevan et al., 2008; Xiao et al., 2004a).

In the WRF-GHG, the simulation of the NEE includes two components: light-driven gross ecosystem exchange (GEE) and temperature-driven ecosystem respiration (R_{eco}). The calculation formulas are as follows:

$$NEE = -\lambda \times T_{scale} \times W_{scale} \times P_{scale} \times EVI \times \frac{1}{(1+PAR/PAR_0)} \times PAR + \alpha \times T + \beta\,, \quad (1)$$

where λ denotes light use efficiency (units: μmol CO_2 m^{-2} s^{-1}/μmol PAR·m^{-2} s^{-1}), and PAR_0 denotes the half-saturation light intensity (unit: μmol PAR·m^{-2} s^{-1}). T represents the 2-m air temperature (unit: ℃), while α and β are respiration-related fitting parameters (units: μmol CO_2 m^{-2} s^{-1}·℃$^{-1}$ and μmol CO_2 m^{-2} s^{-1}, respectively) denoting the temperature sensitivity of ecosystem respiration and the basal respiration rate under extreme cold, respectively.

These four parameters (λ, PAR_0, α, and β) are all key for the estimation of vegetation ecosystem photosynthesis and respiration in the VPRM model. PAR refers to photosynthetically active radiation (μmol PAR·m^{-2} s^{-1}), calculated from the model's downward shortwave radiation. T_{scale}, P_{scale}, and W_{scale} are scaling factors representing the effects of temperature, phenology, and water stress on photosynthesis, respectively. The formulas used to calculate the EVI, the scaling factors, and the LSWI are as follows:

$$EVI = G \times \frac{(\rho_{nir} - \rho_{red})}{\rho_{nir} + (C_1 \times \rho_{red} - C_2 \times \rho_{blue} + L}\,, \quad (2)$$

$$T_{scale} = \frac{(T - T_{\min})(T - T_{\max})}{[(T - T_{\min})(T - T_{\max}) - (T - T_{opt})^2]}\,, \quad (3)$$

$$W_{scale} = \frac{1 + LSWI}{1 + LSWI_{\max}}\,, \quad (4)$$

$$P_{scale} = \frac{1 + LSWI}{2}\,, \quad (5)$$

$$LSWI = \frac{\rho_{nir} - \rho_{swir}}{\rho_{nir} + \rho_{swir}}\,. \quad (6)$$

In Equation (2), G = 2.5, C_1 = 6, C_2 = 7.5, and L = 1. ρ denotes the surface albedo of the corresponding band, with subscripts *nir*, *red*, *blue*, and *swir* representing the near-infrared (841–876 nm), red (620–670 nm), blue (459–479 nm), and shortwave infrared (1628–1652 nm) bands, respectively.

In Equations (3)–(6), T denotes air temperature (℃), while $T_{\min}$, $T_{\max}$, and T_{opt} represent the minimum, maximum, and optimum temperatures for photosynthesis, respectively. When the air temperature is below $T_{\min}$, T_{scale} is set to 0 (Xiao et al., 2004a, 2004b).

https://doi.org/10.5194/egusphere-2025-6272
Preprint. Discussion started: 31 December 2025

2.2 WRF-GHG model configuration

The WRF-GHG model was configured with three nested domains (Figure 1) to simulate the spatiotemporal distribution of atmospheric CO_2 in the PRD region. The outermost domain (d01) covered the South China Sea, East Asia, and mainland China, with a horizontal grid resolution of 36 km. Domain 2 (d02) encompassed southern China (12-km horizontal grid resolution), while Domain 3 (d03) covered the PRD region (4-km horizontal grid resolution).

The WRF-GHG developed in this study included 41 vertical levels with unequal stratification. The first layer had a height of approximately 15 m, and the top layer was at approximately 50 hPa. The physical parameterization schemes of the WRF-GHG and key photosynthesis/respiration parameters of the VPRM were configured with reference to previous studies (Mai et al., 2024), with details provided in Tables 1 and 2.

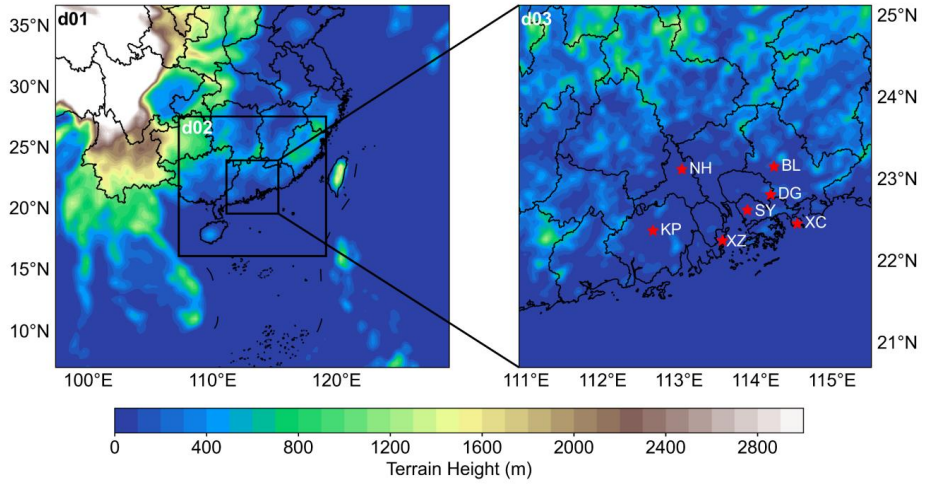

Figure 1. Simulation area of the weather research and forecasting–greenhouse gas model (WRF-GHG). d01: Domain 1 (36-km spatial resolution); d02: Domain 2 (12-km spatial resolution); d03: Domain 3 (4-km spatial resolution). The color bar represents topographic elevation. NH: Nanhai Station, KP: Kaiping Station, XZ: Xiangzhou Station, SY: Shiyan Station, DG: Dongguan Station, BL: Boluo Station, XC: Xichong Station.

Table 1. Weather research and forecasting–greenhouse gas (WRF-GHG) model configurations

Attribute	Model configuration	Reference
Shortwave radiation	Dudhia algorithm	Dudhia (1989)
Longwave radiation	Rapid radiative transfer model (RRTM)	Iacono et al. (2008)
Boundary layer	Yonsei University (YSU) scheme	Hong et al. (2006)
Microphysics	WSM3	Hong et al. (2004)
Cumulus	Kain–Fritsch (first and second nested regions)	Kain (2004)
Land surface model	Noah land-surface scheme	Chen and Dudhia (2001)
Vertical levels	41	
Model top	50 hPa	
Horizontal resolution	36 km × 12 km × 4 km	

https://doi.org/10.5194/egusphere-2025-6272
Preprint. Discussion started: 31 December 2025

Time step	72 s

Table 2. Vegetation photosynthesis and respiration model (VPRM) parameters utilized in this study

	Evergreen forest	Deciduous forest	Mixed forest	Shrub	Savanna	Crop	Grass
α	0.242	0.326	0.342	0.024	0.005	0.071	0.027
β	0.189	0.00	0.00	0.00	0.00	1.65	0.00
λ	0.233	0.173	0.255	0.087	0.114	0.154	0.133
PAR_0	316.29	324.00	206.00	363.00	682.00	421.16	157.00

* PAR_0 units are μmol m^{-2} s^{-1}; λ units are μmol (CO_2) m^{-2} s^{-1}/μmol (PAR) m^{-2} s^{-1}; α units are μmol (CO_2) m^{-2} s^{-1} ℃$^{-1}$; and β units are μmol (CO_2) m^{-2} s^{-1}.

2.3 4D-LETKF carbon assimilate algorithm

The local ensemble transform Kalman filter (LETKF) is an improved version of the traditional EnKF, while the 4D-LETKF is an extended version developed to handle asynchronous observational data (Dai et al., 2019; Hunt et al., 2007). In this study, 4D-LETKF was coupled with WRF-GHG to assimilate hourly CO_2 concentration observations. This section provides a brief overview of the LETKF's basic framework; for details on the LETKF algorithm, refer to Hunt et al. (2007).

In the LETKF, the ensemble analysis mean value $\bar{x}^a$ for each grid is determined according to the following equation:

$$\bar{x}^a = \bar{x}^b + X^b \bar{w}^a, \quad (7)$$

where $\bar{x}^b$ represents anthropogenic carbon emissions, which are derived from the 2022 assessment data provided by EDGAR V7.0, with an associated uncertainty of 95%. The background ensemble perturbation matrix is generated through spatiotemporal correlation perturbation. In the equation, X^b denotes the background ensemble perturbation matrix of each ensemble member, while $\bar{w}^a$ is the mean value of the analysis field weight function. The expression of X^b in this study is as follows:

$$X^b = x^{b(i)} - \bar{x}^b, \{i = 1,2, \dots, k\}, \quad (8)$$

where k denotes the ensemble member. The value of $\bar{w}^a$ can be calculated using the following equation:

$$\bar{w}^a = \tilde{P}^a (Y^b)^T R^{-1} (y^0 - \bar{y}^b), \quad (9)$$

where R denotes the observation error covariance matrix, while y^0 and $\bar{y}^b$ represent the observed values and the ensemble-averaged background observations, respectively. The ensemble background observations are calculated by applying the observation operator H to the ensemble member state vectors $x^{b(i)}$, i.e., $y^{b(i)} = H(x^{b(i)})$. The ensemble background observation perturbations Y^b can be derived from $y^{b(i)}$ and $\bar{y}^b$, with the expression given as follows:

$$Y^b = y^{b(i)} - \bar{y}^b, \{i = 1,2, \dots, k\}. \quad (10)$$

Therefore, the error covariance of the analysis field $\tilde{P}^a$ can be calculated using the following equation:

https://doi.org/10.5194/egusphere-2025-6272
Preprint. Discussion started: 31 December 2025

$$\tilde{P}^a = [(Y^b)^T R^{-1} Y^b + (k-1)I/\rho]^{-1}, \quad (11)$$

where I denotes the indicator matrix, while ρ represents the inflation factor. The ensemble perturbation of the analysis field X^a can be obtained according to the following formula:

$$X^a = X^b[(k-1)\tilde{P}^a]^{1/2}, \quad (12)$$

where the perturbation matrix of the i-th column is $x^a(i) - \bar{x}^a, \{i = 1,2,\dots,k\}$.

In ensemble analysis, optimal anthropogenic carbon emission estimates are generated by adding $\bar{x}^a$ to each column of X^a. The overall framework incorporates two iteratively coupled steps: ensemble forecasting and state analysis. For the assimilation of hourly ground-based CO_2 observations, LETKF requires switching between observation data assimilation and forward simulation.

The 4D-LETKF characterizes the trajectory of the real system based on linear combinations of model background ensemble trajectories and compares these trajectories with observations collected within the assimilation time window (Hunt et al., 2007). This method can be employed to assimilate asynchronous observation data while avoiding frequent switching between the assimilation process and model ensemble forecasting.

The assimilation window in this study was set to 72 h. Within this window, 4D-LETKF performed a 120-h ensemble forecast, outputting hourly results. The first 24 h served as model spin-up with no assimilation. For each hour, simulated background observations and observation biases were calculated simultaneously. Background observation means and perturbation matrices generated for each hourly interval were vertically concatenated to form combined matrices of background observation means and perturbations (Hunt et al., 2007), which were utilized to compute the weight matrix $\bar{w}^a$. This $\bar{w}^a$, which was derived from hourly 12-h lag observation updates within the assimilation window, was applied to the state vector of each hourly period within the window (Di Tomaso et al., 2017).

2.4 Meteorological data, a priori sources, and CO_2 concentration observation data

2.4.1 Sources of meteorological fields and a priori sources

The initial meteorological fields and boundary conditions driving the GRACES-GHG-DA in this study were obtained from the third-generation reanalysis product of the National Centers for Environmental Prediction (NCEP; rda.ucar.edu/datasets/ds083.2/). This product has a temporal resolution of 6 h, with a horizontal resolution of 0.25 °×0.25 °for the first layer and 0.5 °×0.5 ° for the remaining layers. The initial and boundary conditions for the CO_2 concentration fields (including the total CO_2 concentration, background CO_2 concentration, concentration from terrestrial biosphere exchange, the concentration generated by wildfires, concentration resulting from fossil-fuel combustion, and concentration contributed by air-sea exchange) were obtained from the CarbonTracker products (CT2022, CarbonTracker CT2022 - NOAA Global Monitoring Laboratory) (Peters et al., 2007).These products feature a temporal resolution of 3 hours, a spatial resolution of 3 °×2 °, and 34 vertical layers. CT's prior concentration fields include total CO_2 concentration, as well as contributions from

https://doi.org/10.5194/egusphere-2025-6272
Preprint. Discussion started: 31 December 2025

the biosphere, wildfire emissions, and fossil fuel emissions. Prior anthropogenic CO_2 emissions were obtained from the Emission Database for Global Atmospheric Research (EDGAR) v7.0 (EDGAR - The Emissions Database for Global Atmospheric Research (europa.eu)), with a spatial resolution of 0.1 °×0.1 °. CO_2 fluxes from vegetation photosynthesis and respiration were calculated online using the VPRM.

2.4.2 CO_2 concentration observation data

Atmospheric CO_2 concentration observations were collected from seven high-precision stations in the PRD region: Boluo (BL), Dongguan (DG), Kaiping (KP), Nanhai (NH), Shiyan (SY), Xiangzhou (XZ), and Xichong (XC). The locations of these stations are shown in Figure 1. Stations SY, XZ, and XC utilized high-precision greenhouse gas monitoring systems based on cavity ring-down spectroscopy (PICARRO), while the remaining stations employed systems based on off-axis integrated cavity output spectroscopy (LGR). The CO_2 concentration observation accuracy at each station was greater than 0.1 ppm.

All observations were subjected to rigorous quality control, including extreme value screening, cavity temperature checks, cavity pressure checks, humidity checks, and T-value quality control (Fang et al., 2014). Figure S1 shows the distribution of quality-controlled data for each station.

2.5 Anthropogenic CO_2 emission inventory

To compare and validate the top-down atmospheric CO_2 inversion inventory against bottom-up statistical inventories, this study utilized three anthropogenic CO_2 emission statistical inventories in addition to the EDGAR V7.0 inventory. These included the ODIAC v2023 inventory (https://www.odiac.org/index.html), the GCP-GridFEDv2023.1 inventory(http://opendap.uea.ac.uk:8080/opendap/hyrax/greenocean/GridFED/GridFEDv2023.1/contents.html), and the MEICv2.0 inventory (http://meicmodel.org.cn). The spatial resolutions of the ODIAC v2023, GCP-GridFEDv2023.1, and MEIC inventories are 0.01 ° × 0.01 °, 0.1 ° × 0.1 °, and 0.25 ° × 0.25 °, respectively.

3 Validation and analysis of multi-spatiotemporal scale CO_2 inversion concentrations

3.1 Validation of hourly CO_2 concentrations

The CO_2 concentrations inverted using the regional kilometer-scale carbon assimilation system (GRACES-GHG-DA) based on coupling the WRF-GHG and 4D-LETKF across domains d01 through d03 were evaluated against high-precision observations. The model's performance, quantified by the correlation coefficient (R), bias, and root mean square error (RMSE) between simulated and observed values before and after assimilation, is presented in Figures 2, 3, and 4. For the forward simulations (prior to assimilation), domain d01 exhibited a mean R of 0.61, a bias of −11.98 ppm, and an RMSE of 17.11 ppm. The mean R, bias, and RMSE were 0.59, −12.07 ppm, and 17.21 ppm for d02, respectively, and 0.58, −12.23

https://doi.org/10.5194/egusphere-2025-6272
Preprint. Discussion started: 31 December 2025

ppm, and 17.38 ppm for d03, respectively. After assimilation, the R between the simulated and observed CO_2 concentrations increased at each station, while both the bias and the RMSE decreased markedly. Specifically, the mean R, bias, and RMSE became 0.69, 0.17 ppm, and 11.96 ppm for d01, respectively; 0.68, −0.10 ppm, and 12.03 ppm for d02, respectively; and 0.66, −1.03 ppm, and 12.29 ppm for d03, respectively. The differences in these metrics across domains d01–d03 following assimilation were not statistically significant (P < 0.01). The results demonstrated that data assimilation enabled GRACES-GHG-DA to accurately simulate the spatial and temporal variations of atmospheric CO_2 across scales of 36 to 4 km in the PRD. The high-resolution d03 domain, in particular, captured the kilometer-scale characterization of CO_2 evolution (Ahmadov et al., 2009; Diao et al., 2015; Pillai et al., 2011).

In domain d03, GRACES-GHG-DA assimilation enhanced the hourly CO_2 correlation (R) by 0.09 relative to the forward simulation, while the bias and RMSE declined by 10.8 ppm and 4.97 ppm, respectively (Figures S2 and S3). The post-assimilation bias of < 1.0 ppm outperformed satellite-based monitoring (e.g., GOSAT and OCO) (Butz et al., 2011; Mustafa et al., 2021). This bias was comparable to the hourly bias (0.4 ppm) reported by Guo et al. (2023), but it was substantially lower than the forward simulation biases (−6.4 through −1.04 ppm) obtained in previous WRF-GHG studies (Diao et al., 2015; Dong et al., 2021; Hu et al., 2021; Mai et al., 2024; Wang et al., 2023). These improvements demonstrate that optimizing anthropogenic emissions through GRACES-GHG-DA yields atmospheric CO_2 concentrations that are more consistent with observations.

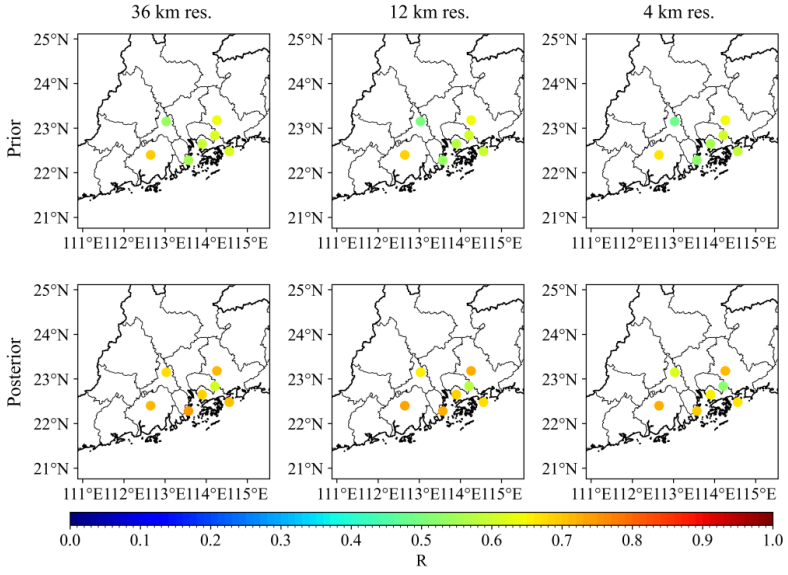

Figure 2. Correlation coefficients (R) between simulated and observed CO_2 concentrations obtained using the regional kilometer-scale carbon assimilation system (Guangzhou Regional Atmospheric Composition and Environment Forecasting System–Greenhouse Gas–Data Assimilation, GRACES-GHG-DA) developed in this study at different grid resolutions (36,

https://doi.org/10.5194/egusphere-2025-6272
Preprint. Discussion started: 31 December 2025

12, and 4 km). The color bar denotes the magnitude of R. In the figure, "Prior" refers to forward simulations, "Posterior" denotes post-assimilation results, and "res." is the abbreviation for "resolution."

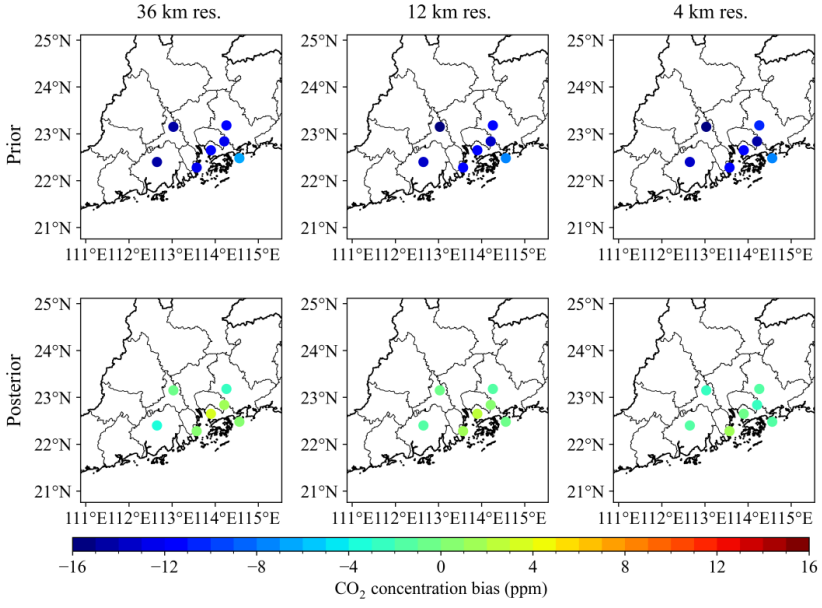

Figure 3. Biases between simulated and observed CO_2 concentrations obtained using the regional kilometer-scale carbon assimilation system (Guangzhou Regional Atmospheric Composition and Environment Forecasting System–Greenhouse Gas–Data Assimilation, GRACES-GHG-DA) developed in this study at different grid resolutions (36, 12, and 4 km). The color bar denotes the magnitude of biases. In the figure, "Prior" refers to forward simulations, "Posterior" denotes post-assimilation results, and "res." is the abbreviation for "resolution."

https://doi.org/10.5194/egusphere-2025-6272
Preprint. Discussion started: 31 December 2025

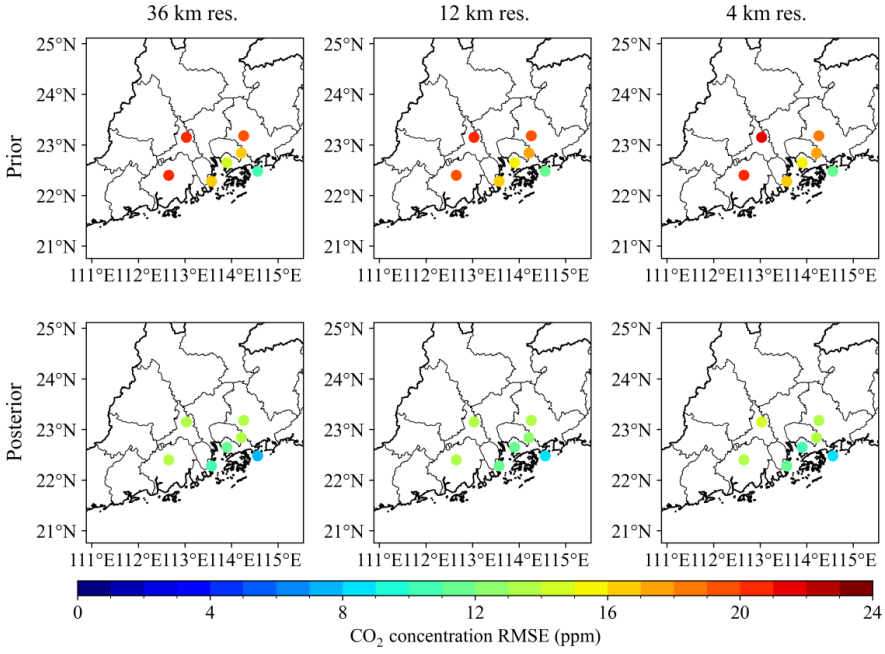

Figure 4. Root mean square error (RMSE) between simulated and observed CO_2 concentrations obtained using the regional kilometer-scale carbon assimilation system (Guangzhou Regional Atmospheric Composition and Environment Forecasting System–Greenhouse Gas–Data Assimilation, GRACES-GHG-DA) developed in this study at different grid resolutions (36, 12, and 4 km). The color bar denotes the magnitude of RMSE. In the figure, "Prior" refers to forward simulations, "Posterior" denotes post-assimilation results, and "res." is the abbreviation for "resolution."

3.2 Validation of the monthly CO_2 concentration assimilation using GRACES-GHG-DA

Figure 5 presents the monthly validation of atmospheric CO_2 concentrations inverted using the GRACES-GHG-DA system in the PRD region. The forward simulations (prior to assimilation) reproduced the observed monthly trends at each station but systematically underestimated the concentrations, likely due to underestimated emissions in the EDGAR inventory. After observations were assimilated to update anthropogenic emissions, the GRACES-GHG-DA system improved the simulation of both the monthly CO_2 variation trends and CO_2 concentrations. The observed annual mean CO_2 across seven stations was 437.92 ppm, compared to 426.54 ppm (forward) and 437.91 ppm (assimilation). This enhancement reduced the annual mean bias from −11.38 ppm to −0.01 ppm, which was superior to the −1.36 ppm bias reported by Mai et al. (2024) for the PRD.

The 1:1 scatter plots of monthly CO_2 concentrations (Figure 6) revealed significant improvement following assimilation. The statistics for GRACES-GHG-DA shifted from an R of 0.81, a bias of −11.59 ppm, and an RMSE of 12.84 ppm to an R of 0.88, a bias of −0.51 ppm, and an RMSE of 4.10 ppm. The regression slope increased from 0.39 to 0.90, and the intercept

https://doi.org/10.5194/egusphere-2025-6272
Preprint. Discussion started: 31 December 2025

decreased from 255.52 to 42.28. These results demonstrate that data assimilation enables GRACES-GHG-DA to more accurately capture the monthly variations in CO_2 and significantly improves the accuracy of regional atmospheric CO_2 simulations.

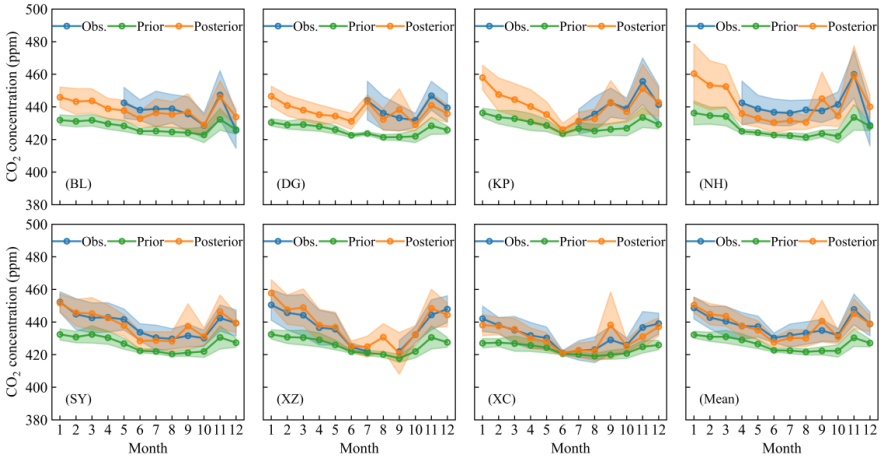

Figure 5. Monthly distributions of simulated and observed CO_2 concentrations in 2022 obtained using the regional kilometer-scale carbon assimilation system (Guangzhou Regional Atmospheric Composition and Environment Forecasting System–Greenhouse Gas–Data Assimilation, GRACES-GHG-DA) developed in this study. The color bar represents standard deviation. In the figure, "Obs." indicates observation, "Prior" refers to forward simulations, and "Posterior" denotes post-assimilation results.

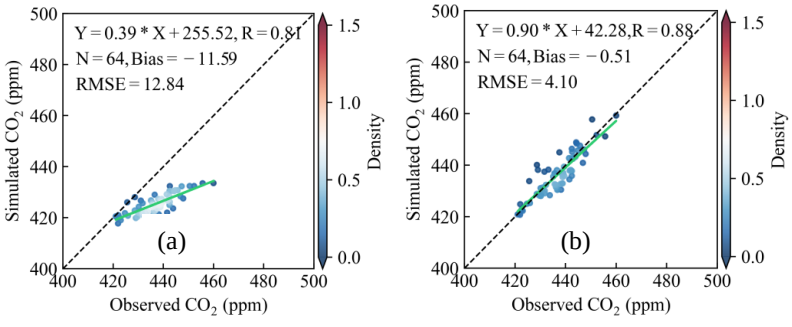

Figure 6. Scatter plots (1:1) of monthly simulated vs. observed CO_2 concentrations. (a) Forward simulations; (b) assimilated inversions.

3.3 Validation of the diurnal CO_2 concentration inverted by GRACES-GHG-DA

To evaluate the performance of GRACES-GHG-DA in simulating regional diurnal CO_2 variations, we compared simulated and observed concentrations across multiple stations (Figure 7). The implementation of 4D-LETKF data assimilation dramatically increased simulation accuracy. Before assimilation, the model exhibited a mean diurnal bias of

https://doi.org/10.5194/egusphere-2025-6272
Preprint. Discussion started: 31 December 2025

−12.24 ppm across all stations, with station-specific biases of −10.99 ppm (BL), −14.13 ppm (DG), −13.90 ppm (KP), −15.56 ppm (NH), −11.73 ppm (SY), −11.96 ppm (XZ), and −7.38 ppm (XC).

Simulation biases were larger at highly polluted urban stations (e.g., DG and NH) than at suburban stations (e.g., BL and SY). This error pattern was closely linked to the complexity of anthropogenic emission sources. Urban areas typically feature more intricate emission mixtures, which can lead to greater model uncertainty. In contrast, suburban areas with lower and less complex emissions generally facilitate more accurate simulations (Lian et al., 2021; Super et al., 2020). For the coastal station XC, the model's ability to represent CO_2 was influenced not only by weaker anthropogenic sources but also by local sea-breeze circulations (Mai et al., 2024). After assimilating CO_2 observations, the diurnal biases across the PRD stations fell to −1.28 ppm (BL), −2.22 ppm (DG), −1.55 ppm (KP), −2.57 ppm (NH), −0.23 ppm (SY), 1.75 ppm (XZ), and −1.13 ppm (XC). The mean bias dropped to −1.53 ppm, an improvement of 10.7 ppm, demonstrating that the GRACES-GHG-DA system effectively mitigated anthropogenic emission uncertainty and enhanced CO_2 simulation accuracy.

Notably, a slight underestimation of CO_2 persisted during morning rush hours in GRACES-GHG-DA simulations, with a mean bias of 0.34 ppm and a value reaching 5.23 ppm at the BL station. This discrepancy was likely due to two factors: the difficulty in resolving complex traffic emissions at high resolution and the challenge of capturing rapid morning changes in meteorological conditions (e.g., solar radiation, temperature, wind, and boundary layer height). For the remainder of the day, simulations showed excellent agreement with observations, with a mean bias of only 0.07 ppm. Biases were persistently higher in high-emission urban areas (e.g., DG and NH) compared to suburban areas (e.g., SY and XC), even after assimilation, highlighting the crucial role of anthropogenic emissions in affecting inversion accuracy in the PRD.

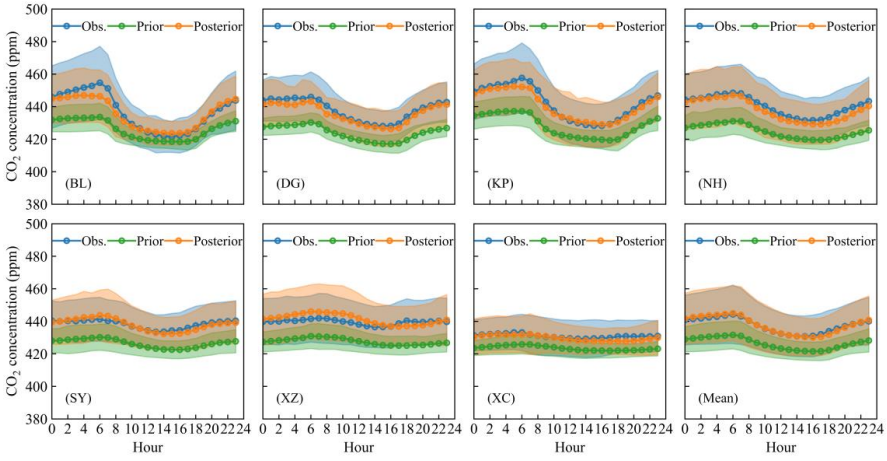

Figure 7. Diurnal distributions of simulated and observed CO_2 concentrations for the regional kilometer-scale carbon assimilation system (Guangzhou Regional Atmospheric Composition and Environment Forecasting System–Greenhouse Gas–Data Assimilation, GRACES-GHG-DA) developed in this study. Colored bars represent the standard deviation. In the

https://doi.org/10.5194/egusphere-2025-6272
Preprint. Discussion started: 31 December 2025

figure, "Obs." indicates observation, "Prior" refers to forward simulations, and "Posterior" denotes post-assimilation results.

3.4 Spatial comparison of CO_2 concentration inverted by GRACES-GHG-DA before and after assimilation

To further evaluate improvements in regional atmospheric CO_2 inversions obtained using the GRACES-GHG-DA system, this study compared the spatial distribution of CO_2 concentrations over the PRD before and after data assimilation (Figure 8). The mean concentration from the forward simulation was 426.97 ppm (Figure 8a). Following assimilation, the inverted value rose to 437.77 ppm (Figure 8b), suggesting that the EDGAR inventory might underestimate regional anthropogenic CO_2 emissions.

In forward simulations, CO_2 concentrations exhibited multiple high-value centers, primarily over Guangzhou, Dongguan, and Foshan, with secondary centers at the Yunfu–Zhaoqing border, the southeastern Qingyuan–southwestern Shaoguan region, and southern Huizhou. These pollution centers corresponded well with pollution sources in the EDGAR inventory. After assimilating CO_2 observations via GRACES-GHG-DA, the multi-center pattern in the PRD region became more distinct. The highest CO_2 concentrations were recorded in the core area (Guangzhou–Dongguan–Foshan–Shenzhen), with a mean of 442.47 ppm, representing an increase of 14.79 ppm over the forward simulation (427.68 ppm; Figure 8c). High-value centers at the Yunfu–Zhaoqing border, southeastern Qingyuan–southwestern Shaoguan, southern Huizhou, Huizhou–Heyuan border, and southern Jiangmen exhibited CO_2 concentrations comparable to the PRD core area, with increments exceeding 20.0 ppm relative to forward simulations (Figure 10c). This spatial distribution reflects the impact on CO_2 concentrations due to recent pollution control policies, which have driven the migration of high-polluting industries from the PRD core to eastern, western, and northern Guangdong (Bian et al., 2019; Mai et al., 2021; Wang et al., 2021).

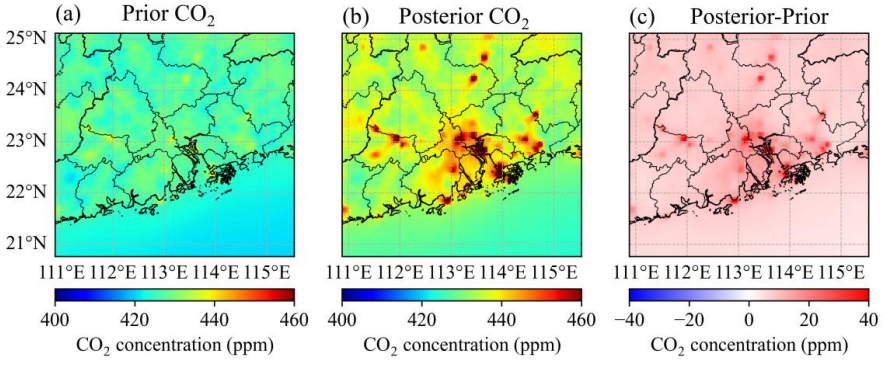

Figure 8. Comparison of 2022 atmospheric CO_2 concentrations in the Pearl River Delta (PRD) region before and after assimilation. (a) Forward simulation; (b) assimilation inversion; (c) differences in CO_2 concentrations before and after assimilation.

https://doi.org/10.5194/egusphere-2025-6272
Preprint. Discussion started: 31 December 2025

4 Spatial distribution of top-down anthropogenic CO_2 emissions in the PRD region and comparison with bottom-up statistical inventories

By assimilating high-precision CO_2 data from greenhouse gas observation stations in the PRD region, the GRACES-GHG-DA system generated a near-real-time top-down anthropogenic CO_2 emission inventory with a 4-km resolution (Figure 9a). In 2022, the total anthropogenic CO_2 emissions inverted for the PRD region were 113.99 Tg C. Across the PRD core area, including Guangzhou, Dongguan, Foshan, and Shenzhen, the average anthropogenic CO_2 emission flux exceeded 7500 g C m^{-2} a^{-1}. Emission hotspots were identified along the Guangzhou–Dongguan, Guangzhou–Foshan, and Shenzhen–Hong Kong borders, where fluxes reached nearly 18,000 g C m^{-2} a^{-1}. Peak emission fluxes above 15,000 g C m^{-2} a^{-1} were also detected in several other areas, including the Zhaoqing–Yunfu border, southeastern Qingyuan–southwestern Shaoguan, southeastern Huizhou, the Huizhou–Heyuan border, southern Jiangmen, and southern Zhuhai. These high fluxes likely reflected emissions from concentrated pollution sources and aligned spatially with elevated CO_2 concentrations (Figure 8b). Outside the PRD core and surrounding high-emission areas, anthropogenic CO_2 fluxes generally remained below 3800 g C m^{-2} a^{-1}. In Zhaoqing, Heyuan, and Yangjiang—excluding a small number of point sources in southwestern Yangjiang—fluxes were below 1000 g C m^{-2} a^{-1}.

The regional CO_2 inversion inventory is compared with four bottom-up statistical inventories in Figure 9b. For 2022, the total CO_2 emissions in the PRD region obtained from the EDGAR, GCP, ODIAC, and MEIC inventories were 94.51, 127.86, 103.02, and 72.08Tg C, respectively. Collectively, the mean value of these inventories (99.37 Tg C) was 14.71% lower than the inversion estimate. The MEIC inventory showed the largest discrepancy, with an underestimation of 36.77%.

Spatially, the EDGAR inventory primarily underestimated emissions in the PRD core area by over 1,500 g C m^{-2} a^{-1}. Underestimations exceeding 700 g C m^{-2} a^{-1} were also detected in northeastern Jiangmen, Zhongshan, the Yunfu–Zhaoqing border, southern Huizhou, central Shaoguan, and southern Shanwei. In contrast, the EDGAR inventory agreed well with the inversion inventories for Maoming, Yangjiang, Shaoguan, Meizhou, Jieyang, and Shantou, with minor differences ranging from −130 to 130 g C m^{-2} a^{-1}.

Similar to EDGAR, the MEIC inventory exhibited a greater underestimation of CO_2 fluxes, with the magnitude exceeding 2,000 g C m^{-2} a^{-1} in Guangzhou, Dongguan, and Shenzhen. Additional underestimations were mainly scattered as point sources outside the PRD core area, which were potentially associated with concentrated industrial emissions. However, the MEIC inventory overestimated fluxes by nearly 2,000 g C m^{-2} a^{-1} in Foshan, Zhongshan, Zhuhai, central Qingyuan, southern Jiangmen, and northern Huizhou.

In contrast to EDGAR, both the ODIAC and GCP inventories overestimated fluxes by more than 1,000 g C m^{-2} a^{-1} along the borders of southern Guangzhou, Dongguan, and Foshan, while their underestimations were confined to discrete point sources. In regions with relatively low CO_2 emissions (e.g., Qingyuan, Shaoguan, Maoming, Yangjiang, Meizhou,

https://doi.org/10.5194/egusphere-2025-6272
Preprint. Discussion started: 31 December 2025

Jieyang, and Shantou), discrepancies between all statistical inventories and the inversion results were minimal, generally within ±200 g C m^{-2} a^{-1}.

In summary, relative to bottom-up inventories, the inversion inventory derived from GRACES-GHG-DA data assimilation showed more reconciled spatial adjustments. Major discrepancies between this inversion inventory and the four statistical inventories were concentrated in the high-emission urban core of the PRD region, whereas non-core areas showed much closer agreement.

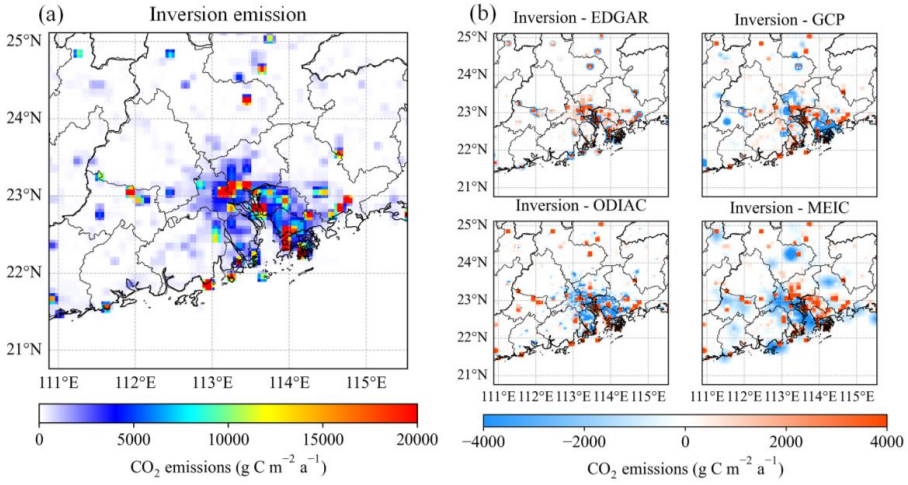

Figure 9. Spatial distribution of the anthropogenic CO_2 inversion inventory and its differences compared to bottom-up inventories in the Pearl River Delta (PRD) region in 2022. (a) Anthropogenic CO_2 inversion inventory obtained in this study; (b) spatial differences between the inversion inventory and four bottom-up statistical inventories (EDGAR, GCP, ODIAC, and MEIC).

In general, inherent uncertainties in sectoral, temporal, and emission factor allocations often limit the ability of bottom-up inventories to depict GHG source–sink dynamics and spatial heterogeneity (Cai et al., 2021). Conversely, the top-down inversion method provides a superior constraint by assimilating high-precision CO_2 observations to optimize a prior bottom-up inventory, thereby enabling the more comprehensive and accurate characterization of regional anthropogenic emissions.

Figure 10 compares the anthropogenic CO_2 emission inventory developed in the present study with four statistical inventories across major cities in the PRD region. The R between the atmospheric CO_2 inversion inventory and the EDGAR statistical inventory reached 0.99, indicating highly consistent variation trends. This strong agreement likely stemmed from the use of the EDGAR inventory as the prior inventory for anthropogenic CO_2 sources in our inversion. Moreover, the linear regression between the inversion and EDGAR inventories showed better agreement in both slope and intercept compared to the other three statistical inventories. In terms of CO_2 emission intensity, the two inventories exhibited good consistency for

https://doi.org/10.5194/egusphere-2025-6272
Preprint. Discussion started: 31 December 2025

values below 10 Tg C a^{-1}. However, as the emission intensity increased, the underestimation by the EDGAR inventory became more pronounced, with an average discrepancy of 5.14 Tg C a^{-1} in high-emission cities such as Guangzhou, Foshan, and Dongguan.

The correlation coefficients (R) between the atmospheric CO_2 inversion inventory and the ODIAC and GCP inventories ranged between 0.74 and 0.80, significantly lower than the correlation with EDGAR (Figure 10b). For emissions at or below 10 Tg C a^{-1}, both ODIAC and GCP produced lower estimates than the inversion inventory. At emissions exceeding 20 Tg C a^{-1}, however, their estimates were generally higher. In contrast, the MEIC inventory showed the weakest correlation (R = 0.72). MEIC systematically underestimated emissions across all regions, with an average underestimation of 9.67 Tg C a^{-1} in high-emission cities including Guangzhou, Dongguan, and Foshan.

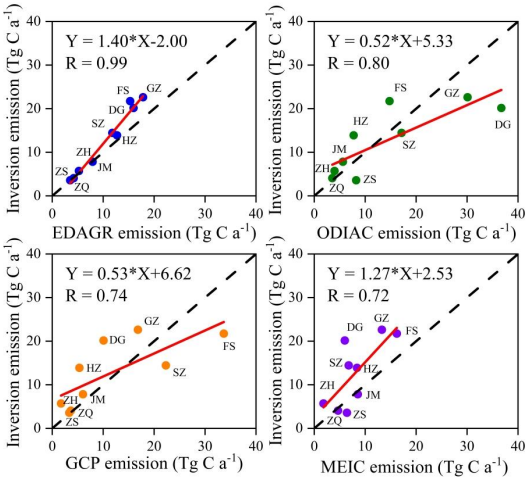

Figure 10. Comparison of the anthropogenic CO_2 inversion inventory of this study with bottom-up inventories in the Pearl River Delta (PRD) region. (a) EDGAR; (b) ODIAC; (c) GCP; (d) MEIC. City abbreviations: ZS (Zhongshan City), ZQ (Zhaoqing City), ZH (Zhuhai City), JM (Jiangmen City), SZ (Shenzhen City), HZ (Huizhou City), DG (Dongguan City), FS (Foshan City), GZ (Guangzhou City).

5 Spatiotemporal distribution of regional top-down anthropogenic CO_2 emissions and their relationship with CO_2 concentrations

5.1 Seasonal distribution of regional anthropogenic CO_2 emissions

Seasonal variations in regional anthropogenic CO_2 emissions arise from multiple factors, including differences in fossil fuel combustion, variations in climate conditions, and fluctuations in vehicle emissions. Figure 11 illustrates the inverted seasonal distribution of anthropogenic CO_2 emissions for the PRD region in 2022. The total anthropogenic CO_2 emissions during spring, summer, autumn, and winter were 24.30, 30.18, 30.66, and 27.06 Tg C, respectively. Spatial distributions

https://doi.org/10.5194/egusphere-2025-6272
Preprint. Discussion started: 31 December 2025

(Figure 12) showed consistent patterns across the four seasons. Within PRD core regions, the mean anthropogenic CO_2 flux surpassed 7000 g C m^{-2} a^{-1}, with high-emission peaks approaching 28000 g C m^{-2} a^{-1} in areas including the Guangzhou–Foshan border, western Dongguan, and the Shenzhen–Hong Kong border. Additionally, discrete high-emission point sources were identified at the Zhaoqing–Yunfu border, central and northern Qingyuan, southern Shaoguan, southern Jiangmen, and southern Huizhou, where CO_2 fluxes exceeded 6000 g C m^{-2} a^{-1}. This pattern may be attributed to emissions from local industrial facilities. In contrast, anthropogenic CO_2 fluxes in Yangjiang, central and northern Zhaoqing, central Huizhou, and Meizhou remained below 1000 g C m^{-2} a^{-1}.

The seasonal comparison of regional anthropogenic emission sources (Figure S4) revealed that anthropogenic CO_2 emission fluxes in spring were generally lower than those in other seasons. Specifically, regions with lower fluxes in spring relative to summer and autumn were primarily concentrated in southern Guangzhou and its border with Foshan, where CO_2 differences approached 5000 g C m^{-2} a^{-1}. In southern Guangzhou, spring anthropogenic CO_2 fluxes were nearly 4500 g C m^{-2} a^{-1} lower than those in winter. In contrast, in areas including the Guangzhou–Foshan border and central Huizhou, spring CO_2 fluxes were approximately 2500 g C m^{-2} a^{-1} higher than those during winter.

Anthropogenic CO_2 emissions in the PRD region peaked in autumn. The largest seasonal increase, reaching 7500 g C m^{-2} a^{-1} compared to spring and winter, occurred in Foshan, central–southern Guangzhou, and the Guangzhou–Foshan border. In contrast, areas with lower autumn emissions relative to winter were primarily located at the Yunfu–Zhaoqing border, southern Shenzhen, and western Dongguan, with a maximum decline of 2500 g C m^{-2} a^{-1}. A notable contrast was also found within the Guangzhou–Foshan area: southern Guangzhou showed a 5000 g C m^{-2} a^{-1} increase in autumn over summer, whereas the Guangzhou–Foshan border experienced a reduction of about 2500 g C m^{-2} a^{-1}.

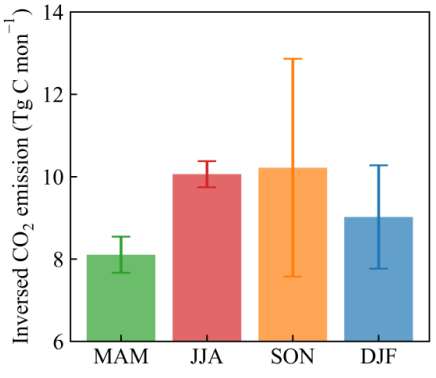

Figure 11. Seasonal distribution of anthropogenic CO_2 emissions in the Pearl River Delta (PRD) region for 2022. MAM, JJA, SON, and DJF denote March–May, June–August, September–November, and December–February, respectively.

https://doi.org/10.5194/egusphere-2025-6272
Preprint. Discussion started: 31 December 2025

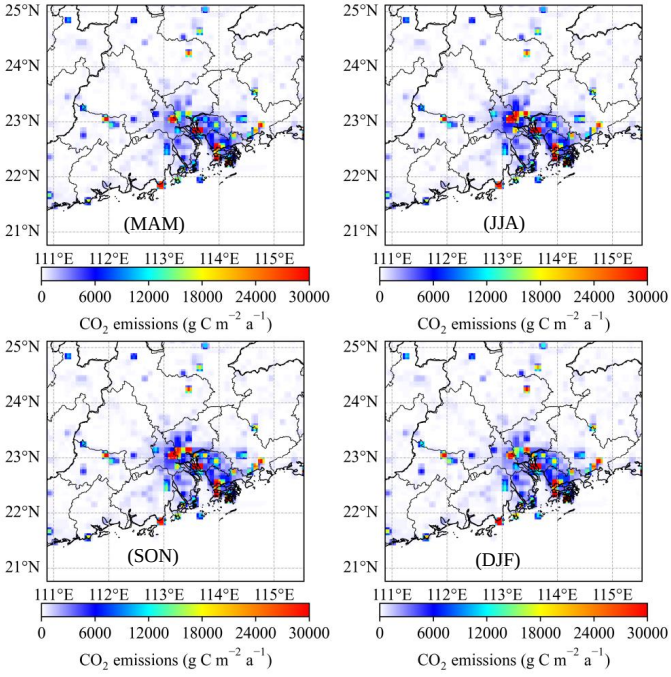

460 Figure 12. Spatial distribution of anthropogenic CO_2 emission fluxes in the Pearl River Delta (PRD) region for 2022. MAM, JJA, SON, and DJF denote March–May, June–August, September–November, and December–February, respectively. The color bar represents CO_2 emissions.

5.2 Diurnal variation of regional anthropogenic CO_2 emissions and their interaction with CO_2 concentrations

The inversion of diurnal CO_2 variations represents a key challenge in regional–urban carbon flux analysis, as current
465 methodological capabilities are largely restricted to daily and weekly temporal resolution (Bréon et al., 2015; Wu et al., 2016). This limitation hinders the quantification of diurnal CO_2 variations and prevents the dynamic adjustment of carbon sources and sinks in urban regions. This is partly due to insufficient hourly CO_2 concentration observations in high-emission urban areas and partly due to the urgent need to develop hourly carbon flux prediction operators for inversion models (Peng et al., 2022; Kou et al., 2024). In the present study, we address these issues by coupling WRF-GHG with 4D-LETKF to
470 assimilate hourly CO_2 observations across the PRD region, thereby producing near dynamically updated CO_2 ensemble forecasts and analysis fields.

Figure 13a depicts the diurnal cycle of CO_2 emissions in the PRD region for 2022. A single-peak pattern was observed across all seasons, with mean fluxes of 1.10, 1.37, 1.40, and 1.25 ($\times 10^{-2}$ Tg C hour^{-1}) in spring, summer, autumn, and winter, respectively. The lowest emissions were obtained in spring, with a peak of 1.16×10^{-2} Tg C hour^{-1} and the smallest
475 amplitude (peak-to-trough difference: 1.16×10^{-2} Tg C hour^{-1}). This seasonal minimum is likely attributed to moderate temperatures, which reduce the demand for high-power appliances such as air conditioners, coupled with lower

https://doi.org/10.5194/egusphere-2025-6272
Preprint. Discussion started: 31 December 2025

manufacturing activity. Previous studies indicate that industry and power plants, the primary consumers of fossil fuels, contribute 75%–90% of the anthropogenic CO_2 emissions in the PRD region (Mai et al., 2021).

A distinct summer peak in anthropogenic CO_2 emissions of 1.48×10^{-2} Tg C hour^{-1} was observed in the PRD region between 09:00 and 12:00 local standard time (LST), with a diurnal amplitude of 0.23×10^{-2} Tg C hour^{-1}. This surge coincides with high cooling demand under hot and humid conditions (apparent temperatures of up to 40 ℃), which significantly increases electricity consumption from fossil fuels. According to statistics, thermal power generation in Guangdong Province during the summer of 2022 reached 107.54 billion kWh, second only to that in the autumn (with electricity consumption of 116.49 billion kWh) (National Bureau of Statistics of China, 2023).

Temperatures in the PRD region remain high during autumn, coinciding with the peak season for manufacturing industries including electronics, apparel, and automobiles. Energy demand from industrial enterprises and power plants reaches its annual peak, driving regional anthropogenic CO_2 emissions to their highest level. Consequently, the results showed that the diurnal CO_2 flux attained a maximum value of 1.55×10^{-2} Tg C hour^{-1}, with the peak persisting from 10:00 to 14:00 LST, indicating robust economic activity.

In winter, the regional anthropogenic CO_2 flux peaked at 1.36×10^{-2} Tg C hour^{-1}, primarily between 09:00 and 12:00 LST, with a diurnal amplitude of 0.20×10^{-2} Tg C hour^{-1}. This pattern was likely influenced by two factors. First, although winter temperatures in the PRD typically remain above 15 ℃, with rare sub-zero periods, heating demand from electrical appliances still causes short-term load increases. Second, the significant peak-to-off-peak electricity price differential in core cities may prompt some industries to shift production schedules to reduce costs. Collectively, these factors lead to substantially lower energy demand and consequent CO_2 emissions during winter than during autumn.

Previous studies have demonstrated that anthropogenic emissions, particularly motor vehicle emissions, are the primary source and main driver of the diurnal variation of atmospheric CO_2 concentrations (Mai et al., 2021). To comprehensively understand the correlation between anthropogenic emissions and CO_2 concentrations in the PRD region, we analyzed the seasonal distributions of diurnal CO_2 emissions and concentrations (Figure 13b). The regional CO_2 concentrations exhibited a diurnal cycle with a consistent bimodal structure across all seasons, distinct from the unimodal pattern of anthropogenic emissions. Seasonal mean CO_2 concentrations were the highest in winter (445.02 ppm), moderate in spring and autumn (437.21 ppm and 437.55 ppm, respectively), and the lowest in summer (429.03 ppm), with peaks occurring between 05:00–07:00 and 21:00–23:00 LST.

In contrast, the diurnal structures of anthropogenic CO_2 emissions and CO_2 concentrations differed markedly across seasons. Anthropogenic emissions were comparable in summer and autumn, followed by lower emissions in winter and the lowest emissions in spring. This seasonal ranking of emissions differed significantly from the seasonal pattern of CO_2 concentrations. These results suggest that anthropogenic emissions are not the dominant factor regulating CO_2

https://doi.org/10.5194/egusphere-2025-6272
Preprint. Discussion started: 31 December 2025

concentrations in the study region. Our study hypothesizes that, in addition to anthropogenic carbon emissions, factors including vegetation conditions, boundary layer structure, and regional atmospheric transport may also exert important regulatory effects on CO_2 concentrations. To verify this hypothesis, we analyzed the relationships between CO_2 concentrations and factors including anthropogenic CO_2 emission sources, natural sinks, and planetary boundary layer height (PBLH) (Figure 13). The highest mean diurnal concentration occurred in winter (Figure 13b), despite intermediate emission levels (Figure 13a). This was likely due to the weakest net carbon uptake by vegetation (Figure 13c) and the lowest PBLH (Figure 13d), both of which favored local CO_2 accumulation. Additionally, driven by winter monsoon winds, the cross-regional transport of CO_2 from high-latitude areas further increased CO_2 concentrations in the PRD region (Figure S5). In contrast to winter, summer exhibited the lowest CO_2 concentration (Figure 13b), although its anthropogenic carbon emissions were comparable to those in autumn. This was attributed to stronger vegetation uptake (Figure 13a, c), which offset anthropogenic sources, and a higher PBLH, which enhanced dispersion (Figure 13d). Furthermore, summer southwestern monsoon winds imported air with lower CO_2 levels from the South China Sea, reducing local concentrations (Figure S5).

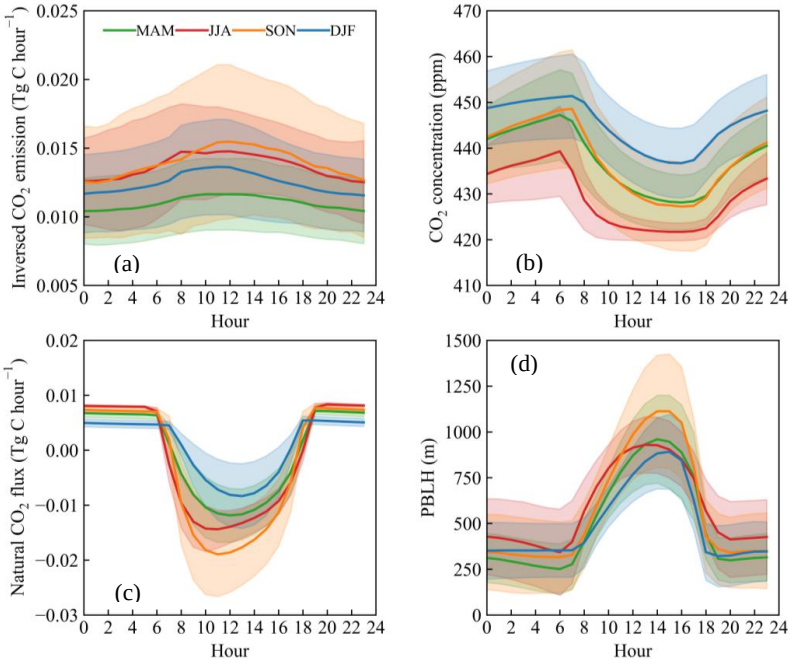

Figure 13. Diurnal variation characteristics of (a) CO_2 emission sources, (b) CO_2 concentrations, (c) natural CO_2 fluxes, and (d) planetary boundary layer height (PBLH) in the Pearl River Delta (PRD) region for 2022. MAM, JJA, SON, and DJF denote March–May, June–August, September–November, and December–February, respectively.

https://doi.org/10.5194/egusphere-2025-6272
Preprint. Discussion started: 31 December 2025

6 Conclusions

Climate change adaptation and mitigation in China will require enhanced carbon evaluation capacities. China's national dual carbon goals of achieving peak carbon emissions by 2030 and carbon neutrality by 2060 highlight the need for the reliable verification of emission reductions. Addressing this challenge necessitates the development of high-resolution top-down inversion technologies. These techniques will not only enable the objective quantification of anthropogenic CO_2 sources and natural carbon sinks but will also provide scientific evidence to evaluate the effectiveness of dual-carbon–aligned emission reduction measures while supporting regional initiatives in energy conservation, emission reduction, and climate change mitigation. To address this issue, we developed the GRACES-GHG-DA system by coupling WRF-GHG with 4D-LETKF. This system assimilates CO_2 observation data from seven high-precision greenhouse gas monitoring stations in the PRD region to construct a near-real-time 4-km anthropogenic emission inventory. This inventory enables the analysis of the spatiotemporal distribution of emissions and their association with CO_2 concentrations. The main conclusions of the present study are as follows:

(1) The GRACES-GHG-DA system accurately captures the spatial distribution of atmospheric CO_2 concentrations in the PRD region across resolutions from 36 to 4 km. The assimilation of CO_2 data maintained consistent model performance metrics (R, bias, and RMSE) across resolutions. The 4-km resolution proved superior for resolving meso- and micro-scale CO_2 variations, with simulation biases of −0.77 (hourly), −0.51 (monthly), and 1.51 (diurnally) ppm. Post-assimilation regional CO_2 concentrations were 10.8 ppm higher than those obtained from the forward simulation, generally exhibiting a pattern consisting of high-emission centers over the core PRD regions of Guangzhou–Dongguan–Foshan–Shenzhen accompanied by multiple high-value CO_2 concentration sources in surrounding regions.

(2) The regional top-down CO_2 emission inventory at a resolution of 4 km in the PRD region was generated by assimilating high-precision CO_2 data via the GRACES-GHG-DA system. In 2022, the inverted anthropogenic CO_2 flux in core PRD cities averaged over 7500 g C m^{-2} a^{-1}, whereas peripheral areas (e.g., Zhaoqing, Heyuan, and Yangjiang) exhibited fluxes of less than 1000 g C m^{-2} a^{-1}. The inversion showed strong spatial agreement with the EDGAR inventory (R = 0.99) and moderate correlations (R = 0.72–0.80) with ODIAC, GCP, and MEIC. Furthermore, the mean total emissions obtained from the statistical inventories were 14.71% lower than the inverted estimate, with an underestimation exceeding 1,500 g C m^{-2} a^{-1} in the core urban centers of the PRD region.

(3) Anthropogenic CO_2 emissions in the PRD region during 2022 exhibited a consistent single-peak diurnal pattern across all seasons, with totals of 24.03 Tg C in spring, 29.86 in summer, 30.61 in autumn, and 27.26 in winter. The seasonal minimum in spring was likely attributed to reduced residential electricity demand under moderate temperatures and lower fossil fuel consumption by power plants amid off-peak manufacturing. Conversely, emissions peaked in autumn in

https://doi.org/10.5194/egusphere-2025-6272
Preprint. Discussion started: 31 December 2025

association with elevated household electricity use due to high temperatures and substantial industrial power consumption during the peak manufacturing season for commodities including electronic products, apparel, and automobiles.

(4) CO_2 concentrations in the PRD region exhibited a consistent bimodal diurnal cycle and a distinct seasonal pattern across all seasons, with the highest mean value recorded in winter (445.02 ppm) and the lowest in summer (429.03 ppm). The intermediate mean CO_2 values in spring (437.21 ppm) and autumn (437.55 ppm) were comparable. The significant discrepancy between this concentration pattern and the seasonal profile of anthropogenic emissions suggests that, in addition to direct anthropogenic emissions, processes such as vegetation carbon source–sink dynamics, boundary layer evolution, and regional transport play significant roles in shaping CO_2 concentrations.

Data Availability

- The data used in this study are available on Science Data Bank (https://doi.org/10.57760/sciencedb.34615). Additionally, they can also be made available for scientific purposes upon request to the authors (Boru Mai, mbr4@163.com and Xuejiao Deng, Dengxj@gd121.cn).
- The FNL (Final) Operational Global Analysis data set used for providing initial meteorological fields and boundary conditions for GRACES-GHG-DA model were available at the Research Data Archive (RDA) via https://doi.org/10.5065/D6M043C6.
- The MOD09A1V6.1 product—MODIS/Terra Surface Reflectance 8-Day L3 Global 500 m SIN Grid—was utilized to calculate the EVI and LSWI in the VPRM (Vermote, 2021).
- The initial and boundary conditions for the CO_2 concentration fields were obtained from the CarbonTracker products (CT2022) from https://www.esrl.noaa.gov/gmd/ccgg/carbontracker/(Jacobson et al., 2023).
- Anthropogenic CO_2 emission inventory data were sourced from four databases: EDGAR V7.0 (European Commission & Joint Research Centre, 2022), ODIAC v2023 (Tomohiro and Shamil, 2024), GCP-GridFEDv2023.1(Jones et al., 2023), and MEICv2.0 (Xu et al., 2023).

Author Contributions

BM and YW initiated the study. Model coupling and simulations were carried out by BM and TD (Tie Dai). TD (Tao Deng), XZ, YC, XD, FX, ML, YL, and YZ participated in data analysis. YW wrote the manuscript, which was revised by BM and TD(Tie Dai).

Competing interests

The contact author has declared that none of the authors has any competing interests.

https://doi.org/10.5194/egusphere-2025-6272
Preprint. Discussion started: 31 December 2025

Disclaimer

Publisher's note: Copernicus Publications remains neutral with regard to jurisdictional claims made in the text, published maps, institutional affiliations, or any other geographical representation in this paper. While Copernicus Publications makes every effort to include appropriate place names, the final responsibility lies with the authors.

Acknowledgments

This research was funded by the Youth Innovation Team Plan of the China Meteorological Administration (CMA) (Grant number: CMA2023QN13) , the Guangdong Provincial Natural Science Foundation (Grant numbers: 2022A1515010718 and 2021A1515011494), the Special Project for Innovation Development of the CMA (Grant number: CXFZ2022J047), and the CMA Open Competition Mechanism to Select Best Candidates Project (Grant number: CMAJBGS202218). We thank the developers of the WRF-GHG model for providing the modeling tool. We also extend our appreciation to all field campaign participants for their dedicated work and collaboration. Furthermore, we are indebted to the anonymous reviewers for their constructive feedback that enhanced the manuscript.

Financial support

This research was supported by the Youth Innovation Team Plan of the China Meteorological Administration (CMA) (Grant number: CMA2023QN13), the Guangdong Provincial Natural Science Foundation (Grant numbers: 2022A1515010718 and 2021A1515011494), the Special Project for Innovation Development of the CMA (Grant number: CXFZ2022J047), and the CMA Open Competition Mechanism to Select Best Candidates Project (Grant number: CMAJBGS202218).

References

Ahmadov, R., Gerbig, C., Kretschmer, R., Körner, S., Rödenbeck, C., Bousquet, P., and Ramonet, M.: Comparing high resolution WRF-GHG simulations and two global CO_2 transport models with coastal tower measurements of CO_2, Biogeosciences, 6, 807–817, doi:10.5194/bg-6-807-2009, 2009.

Bian, Y., Huang, Z., Ou, J., Zhong, Z., Xu, Y., Zhang, Z., Xiao, X., Ye, X., Wu, Y., Yin, X., Li, C., Chen, L., Shao, M., and Zheng, J.: Evolution of anthropogenic air pollutant emissions in Guangdong Province, China, from 2006 to 2015, Atmos. Chem. Phys., 19, 11701–11719, doi:10.5194/acp-19-11701-2019, 2019.

Bréon, F. M., Broquet, G., Puygrenier, V., Chevallier, F., Xueref-Remy, I., Ramonet, M., Dieudonné, E., Lopez, M., Schmidt, M., Perrussel, O., and Ciais, P.: An attempt at estimating Paris area CO_2 emissions from atmospheric concentration measurements, Atmospheric Chemistry and Physics, 15, 1707–1724, doi:10.5194/acp-15-1707-2015, 2015.

https://doi.org/10.5194/egusphere-2025-6272
Preprint. Discussion started: 31 December 2025

Butz, A., Guerlet, S., Hasekamp, O., Schepers, D., Galli, A., Aben, I., et al.: Toward accurate CO_2 and CH_4 observations from GOSAT, Geophysical Research Letters, 38(14), L14812, doi:10.1029/2011GL047888, 2011.

Cai, Z., Cheng, L., Li, T., Zheng, X., Wang, L., Han, S., Wang, K., Qu, X., Jiang, F., Zhang, Y., Zhu, J., Long, S., Sun, Y., Jia, B., Yuan, W., Zhang, T., Zhang, Q., Xie, J., Zhu, J., Liu, Z., Wu, L., Yang, D., Wei, K., Wu, L., Zhang, W., Liu, Y., and Cao, J.: Key scientific and technical issues in Earth system science towards achieving carbon neutrality in China, Bulletin of the Chinese Academy of Sciences, 36(05), 602–613, doi:10.16418/j.issn.1000-3045.20210402002, 2021.

Chen, B. Z. and Zhang, H. F.: Research on China's Carbon Assimilation System and Its Applications, Science Press, Beijing, 2015.

Chen, F. and Dudhia, J.: Coupling an Advanced Land Surface–Hydrology Model with the Penn State–NCAR MM5 Modeling System. Part I: Model Implementation and Sensitivity, Mon. Weather Rev., 129, 569–585, doi:10.1175/1520-0493(2001)129<0569:Caalsh>2.0.Co;2, 2001.

Chen, J. M., Ju, W. M., Liu, R. G., Li, Y., and Jiang, F.: Remote sensing and optimized calculation methods for global terrestrial carbon sinks, Science Press, Beijing, 2015.

Cheng, Y., Aa, X., Yun, F., Zhou, L., Liu, L., Fang, S., and Xu, L.: Simulation of CO_2 variations at Chinese background atmospheric monitoring stations between 2000 and 2009: Applying a CarbonTracker model, Chin. Sci. Bull., 58, 3986–3993, doi:10.1007/s11434-013-5895-y, 2013.

Cheng, Y., Dai, T., Goto, D., Schutgens, N. A. J., Shi, G., and Nakajima, T.: Investigating the assimilation of CALIPSO global aerosol vertical observations using a four-dimensional ensemble Kalman filter, Atmos. Chem. Phys., 19, 13445–13467, doi:10.5194/acp-19-13445-2019, 2019.

Dai, T., Cheng, Y., Goto, D., Schutgens, N. A. J., Kikuchi, M., Yoshida, M., Shi, G., and Nakajima, T.: Inverting the East Asian Dust Emission Fluxes Using the Ensemble Kalman Smoother and Himawari-8 AODs: A Case Study with WRF-Chem v3.5.1, Atmosphere, 10, doi:10.3390/atmos10090543, 2019.

Dai, T., Cheng, Y., Suzuki, K., Goto, D., Kikuchi, M., Schutgens, N. A. J., Yoshida, M., Zhang, P., Husi, L., Shi, G., and Nakajima, T.: Hourly aerosol assimilation of Himawari-8 AOT using the four-dimensional local ensemble transform Kalman filter, Journal of Advances in Modeling Earth Systems, 11, 680–711, doi:10.1029/2018MS001475, 2019a.

Di Tomaso, E., Schutgens, N. A. J., Jorba, O., and Pérez García-Pando, C.: Assimilation of MODIS Dark Target and Deep Blue observations in the dust aerosol component of NMMB-MONARCH version 1.0, Geoscientific Model Development, 10(3), 1107–1129, doi:10.5194/gmd-10-1107-2017, 2017.

Diao, Y., Huang, J., Liu, C., et al.: A Modeling Study of CO_2 Flux and Concentrations over the Yangtze River Delta Using the WRF-GHG Model, Chin. J. Atmos. Sci., 39, 849–860, doi:10.1029/2019jd031686, 2015.

Dong, X., Yue, M., Jiang, Y., Hu, X. M., Ma, Q., Pu, J., and Zhou, G.: Analysis of CO_2 spatio-temporal variations in China

https://doi.org/10.5194/egusphere-2025-6272
Preprint. Discussion started: 31 December 2025

using a weather–biosphere online coupled model, Atmos. Chem. Phys., 21, 7217–7233, doi:10.5194/acp-21-7217-2021, 2021.

Dudhia, J.: Numerical Study of Convection Observed during the Winter Monsoon Experiment Using a Mesoscale Two-Dimensional Model, J. Atmos. Sci., 46, 3077–3107, doi:10.1175/1520-0469(1989)046<3077:Nsocod>2.0.Co;2, 1989.

European Commission & Joint Research Centre.: EDGAR (Emissions Database for Global Atmospheric Research) Community GHG database,Global Greenhouse Gas Emissions EDGAR_V8.0[Dataset], https://edgar.jrc.ec.europa.eu/dataset_ghg70, 2022.

Fang, S. X., Zhou, L. X., Tans, P. P., Ciais, P., Steinbacher, M., Xu, L., and Luan, T.: In situ measurement of atmospheric CO_2 at the four WMO/GAW stations in China, Atmos. Chem. Phys., 14, 2541–2554, doi:10.5194/acp-14-2541-2014, 2014.

Gloor, M., Fan, S.-M., Pacala, S., and Sarmiento, J.: Optimal sampling of the atmosphere for purpose of inverse modeling: A model study, Global Biogeochemical Cycles, 14(1), 407–428, doi:10.1029/1999GB900052, 2000.

Guo, L., Zhang, X., Zhong, J., Wang, D., Miao, C., Zhao, L., Zhou, Z., Liao, J., Hu, B., Zhu, L., and Chen, Y.: Construction and application of a regional kilometer-scale carbon source and sink assimilation inversion system (CCMVS-R), Engineering, doi:10.1016/j.eng.2023.02.017, 2024.

Gurney, K. R., Liang, J., Patarasuk, R., O'Keeffe, D., Huang, J., Hutchins, M., Lauvaux, T., Turnbull, J. C., and Shepson, P. B.: Reconciling the differences between a bottom-up and inverse-estimated $FFCO_2$ emissions estimate in a large US urban area, Elementa: Science of the Anthropocene, 5, 44, doi:10.1525/elementa.137, 2017.

Han, P., Zeng, N., Oda, T., Zhang, W., Lin, X., Liu, D., Cai, Q., Ma, X., Meng, W., Wang, G., Wang, R., and Zheng, B.: A city-level comparison of fossil-fuel and industry processes-induced CO_2 emissions over the Beijing-Tianjin-Hebei region from eight emission inventories, Carbon Balance and Management, 15, 25, doi:10.1186/s13021-020-00163-2, 2020.

Han, R. and Tian, X.: A dual-pass carbon cycle data assimilation system to estimate surface CO_2 fluxes and 3D atmospheric CO_2 concentrations from spaceborne measurements of atmospheric CO_2, Geoscientific Model Development, doi:10.5194/gmd-2019-54, 2019.

Hong, S. Y., Dudhia, J., and Chen, S. H.: A Revised Approach to Ice Microphysical Processes for the Bulk Parameterization of Clouds and Precipitation, Mon. Weather Rev., 132, 103–120, doi:10.1175/1520-0493(2004)132<0103:Aratim>2.0.Co;2, 2004.

Hong, S. Y., Noh, Y., and Dudhia, J.: A New Vertical Diffusion Package with an Explicit Treatment of Entrainment Processes, Mon. Weather Rev., 134, 2318–2341, doi:10.1175/Mwr3199.1, 2006.

Hu, X. M., Gourdji, S. M., Davis, K. J., Wang, Q., Zhang, Y., Xue, M., Feng, S., Moore, B., and Crowell, S. M. R.:

https://doi.org/10.5194/egusphere-2025-6272
Preprint. Discussion started: 31 December 2025

Implementation of improved parameterization of terrestrial flux in WRF-VPRM improves the simulation of nighttime CO_2 peaks and a daytime CO_2 band ahead of a cold front, J. Geophy. Res.-Atmos., doi:10.1029/2020JD034362, 2021.

Hunt, B. R., Kostelich, E. J., and Szunyogh, I.: Efficient data assimilation for spatiotemporal chaos: A local ensemble transform Kalman filter, Physica D: Nonlinear Phenomena, 230(1-2), 112–126, doi:10.1016/j.physd.2006.11.008, 2007.

Jacobson, A. R., Schuldt, K. N., Tans, P., Arlyn Andrews, Miller, J. B., Oda, T., et al.: NOAA Global Monitoring Laboratory, CarbonTracker CT2022 [Dataset], https://doi.org/10.25925/Z1GJ-3254, 2023.

Iacono, M. J., Delamere, J. S., Mlawer, E. J., et al.: Radiative forcing by long-lived greenhouse gases: Calculations with the AER radiative transfer models, J. Geophys. Res. Atmos., 113, doi:10.1029/2008JD009944, 2008.

IPCC: 2019 Refinement to the 2006 IPCC Guidelines for National Greenhouse Gas Inventories, https://www.ipcc.ch/report/2019-refinement-to-the-2006-ipcc-guidelines-for-national-greenhouse-gas-inventories/, 2019.

Jiang, F., Wang, H., Chen, J. M., Ju, W., Tian, X., Feng, S., Li, G., Chen, Z., Zhang, S., Lu, X., Liu, J., Wang, H., Wang, J., He, W., and Wu, M.: Regional CO_2 fluxes from 2010 to 2015 inferred from GOSAT XCO2 retrievals using a new version of the Global Carbon Assimilation System, Atmospheric Chemistry and Physics, 21, 1963–1985, doi:10.5194/acp-21-1963-2021, 2021.

Jones, M. W., Andrew, R. M., Peters, G. P., Janssens-Maenhout, G., De-Gol, A. J., Dou, X., Liu, Z., Pickers, P., Ciais, P., Patra, P. K., Chevallier, F., & Le Quéré, C.: Gridded fossil CO_2 emissions and related O_2 combustion consistent with national inventories (GCP-GridFEDv2023.1), Zenodo [Data set], https://doi.org/10.5281/zenodo.8386803, 2023.

Ju, W., Fang, H., Tian, X., Jiang, F., Zhan, W., Liu, Y., Wang, Z., He, J., Wang, S., Peng, S., Zhang, Y., Zhou, Y., Jia, B., Yang, D., Fu, Y., Li, R., Liu, J., Wang, H., Li, G., and Chen, Z.: Achievements of study on the global carbon assimilation system based on multisource remote sensing data, China Basic Science, 21(03), 24–27+35, doi:10.11867/j.issn.1001-8166.2016.11.1105, 2019.

Kain, J. S.: The Kain–Fritsch Convective Parameterization: An Update, J. Appl. Meteorol., 43, 170–181, doi:10.1175/1520-0450(2004)043<0170:Tkcpau>2.0.Co;2, 2004.

Kaminski, T., Knorr, W., Schürmann, G., Scholze, M., Rayner, P. J., Zaehle, S., Blessing, S., Dorigo, W., Gayler, V., Giering, R., Gobron, N., Grant, J. P., Heimann, M., Hooker-Stroud, A., Houweling, S., Kato, T., Kattge, J., Kelley, D., Kemp, S., Koffi, E. N., Köstler, C., Mathieu, P. P., Pinty, B., Reick, C. H., Rödenbeck, C., Schnur, R., Scipal, K., Sebald, C., Stacke, T., van Scheltinga, A. T., Vossbeck, M., Widmann, H., and Ziehn, T.: The BETHY/JSBACH Carbon Cycle Data Assimilation System: experiences and challenges, Journal of Geophysical Research: Biogeosciences, 118, 1414–1426, doi:10.1002/jgrg.20118, 2013.

Kou, X., Peng, Z., Zhang, M., Hu, F., Han, X., Li, Z., and Lei, L.: The carbon sink in China as seen from GOSAT with a

https://doi.org/10.5194/egusphere-2025-6272
Preprint. Discussion started: 31 December 2025

regional inversion system based on the Community Multi-scale Air Quality (CMAQ) and ensemble Kalman smoother (EnKS), Atmos. Chem. Phys., 23, 6719–6741, doi:10.5194/acp-23-6719-2023, 2023.

Kou, X., Peng, Z., Zhang, M., Miao, S., Chen, M., and Zhao, X.: Research progress in urban and regional-scale atmospheric inversions of carbon sources and sinks, Environmental Engineering (China), 42(10), 209–217, doi:10.13205/j.hjgc.202410024, 2024.

Li, X., Hu, X.-M., Cai, C., Jia, Q., Zhang, Y., Liu, J., Xue, M., Xu, J., Wen, R., and Crowell, S. M. R.: Terrestrial CO_2 Fluxes, Concentrations, Sources and Budget in Northeast China: Observational and Modeling Studies, J. Geophys. Res. Atmos., 125, doi:10.1029/2019jd031686, 2020.

Lian, J., Bréon, F.-M., Broquet, G., Lauvaux, T., Zheng, B., Ramonet, M., Xueref-Remy, I., Kotthaus, S., Haeffelin, M., and Ciais, P.: Sensitivity to the sources of uncertainties in the modeling of atmospheric CO_2 concentration within and in the vicinity of Paris, Atmos. Chem. Phys., 21, 10707–10726, doi:10.5194/acp-21-10707-2021, 2021.

Mahadevan, P., Wofsy, S. C., Matross, D. M., Xiao, X., Dunn, A. L., Lin, J. C., Gerbig, C., Munger, J. W., Chow, V. Y., and Gottlieb, E. W.: A satellite-based biosphere parameterization for net ecosystem CO_2 exchange: Vegetation Photosynthesis and Respiration Model (VPRM), Global Biogeochem. Cycles, 22, doi:10.1029/2006gb002735, 2008.

Mai, B., Deng, X., Liu, X., Li, T., Guo, J., and Ma, Q.: The climatology of ambient CO_2 concentrations from long-term observation in the Pearl River Delta region of China: Roles of anthropogenic and biogenic processes, Atmos. Environ., 251, doi:10.1016/j.atmosenv.2021.118266, 2021.

Mai, B., Diao, Y., Yang, H., Deng, T., Zou, Y., Wang, Y., Lan, W., Liu, X., and Deng, X.: Assessing atmospheric CO_2 concentrations and contributions from biogenic and anthropogenic sources in the Pearl River Delta region, Urban Clim., 54, doi:10.1016/j.uclim.2024.101864, 2024.

Masarie, K. A. and Tans, P. P.: Extension and integration of atmospheric carbon dioxide data into a globally consistent measurement record, Journal of Geophysical Research, 100(D6), 11593–11610, doi:10.1029/95JD00859, 1995.

Monteil, G., Broquet, G., Scholze, M., Lang, M., Karstens, U., Gerbig, C., Koch, F.-T., Smith, N. E., Thompson, R. L., Luijkx, I. T., White, E., Meesters, A., Ciais, P., Ganesan, A. L., Manning, A., Mischurow, M., Peters, W., Peylin, P., Tarniewicz, J., Rigby, M., Rödenbeck, C., Vermeulen, A., and Walton, E. M.: The regional European atmospheric transport inversion comparison, EUROCOM: first results on European-wide terrestrial carbon fluxes for the period 2006–2015, Atmospheric Chemistry and Physics, 20, 12063–12091, doi:10.5194/acp-20-12063-2020, 2020.

Mustafa, F., Wang, H., Bu, L., Wang, Q., Shahzaman, M., Bilal, M., Zhou, M., Iqbal, R., Aslam, R. W., Ali, M. A., Qiu, Z., et al.: Validation of GOSAT and OCO-2 against In Situ Aircraft Measurements and Comparison with CarbonTracker and GEOS-Chem over Qinhuangdao, China, Remote Sensing, 13(5), 899, doi:10.3390/rs13050899, 2021.

National Bureau of Statistics of China: Monthly report on industrial energy production in Guangdong

https://doi.org/10.5194/egusphere-2025-6272
Preprint. Discussion started: 31 December 2025

Province, https://data.stats.gov.cn/easyquery.htm?cn=E0101, 2023.

Peng, Z., Zhang, M., Kou, X., Tian, X., and Ma, X.: A regional carbon data assimilation system and its preliminary evaluation in East Asia, Atmospheric Chemistry and Physics, 15, 1087–1104, doi:10.5194/acp-15-1087-2015, 2015.

Peng, Z., Kou, X., Zhang, M., Lei, L., Miao, S., Wang, H., Jiang, F., Han, X., and Fang, S.: CO_2 flux inversion with a regional joint data assimilation system based on CMAQ, EnKS, and surface observations, Journal of Geophysical Research: Atmospheres, 128, doi:10.1029/2022JD037154, 2023.

Peters, W., Jacobson, A. R., Sweeney, C., Andrews, A. E., Conway, T. J., Masarie, K., Miller, J. B., Bruhwiler, L. M. P., Pétron, G., Hirsch, A. I., Worthy, D. E. J., van der Werf, G. R., Randerson, J. T., Wennberg, P. O., Krol, M. C., and Tans, P. P.: An atmospheric perspective on North American carbon dioxide exchange: CarbonTracker, Proceedings of the National Academy of Sciences, 104, 18925–18930, doi:10.1073/pnas.0708986104, 2007.

Peters, W., Krol, M. C., Van Der Werf, G. R., Houweling, S., Jones, C. D., Hughes, J., Schaefer, K., Masarie, K. A., Jacobson, A. R., Miller, J. B., Cho, C. H., Ramonet, M., Schmidt, M., Ciattaglia, L., Apadula, F., Heltai, D., Meinhardt, F., Di Sarra, A. G., Piacentino, S., Sferlazzo, D., Aalto, T., Hatakka, J., StrÖM, J., Haszpra, L., Meijer, H. A. J., Van Der Laan, S., Neubert, R. E. M., Jordan, A., RodÓ, X., Morguí, J. A., Vermeulen, A. T., Popa, E., Rozanski, K., Zimnoch, M., Manning, A. C., Leuenberger, M., Uglietti, C., Dolman, A. J., Ciais, P., Heimann, M., and Tans, P. P.: Seven years of recent European net terrestrial carbon dioxide exchange constrained by atmospheric observations, Global Change Biology, 16, 1317–1337, doi:10.1111/j.1365-2486.2009.02078.x, 2010.

Peylin, P., Law, R. M., Gurney, K. R., Chevallier, F., Jacobson, A. R., Maki, T., Niwa, Y., Patra, P. K., Peters, W., Rayner, P. J., Rödenbeck, C., van der Laan-Luijkx, I. T., and Zhang, X.: Global atmospheric carbon budget: results from an ensemble of atmospheric CO_2 inversions, Biogeosciences, 10, 6699–6720, doi:10.5194/bg-10-6699-2013, 2013.

Pillai, D., Gerbig, C., Ahmadov, R., Rödenbeck, C., Kretschmer, R., Koch, T., Thompson, R., Neininger, B., and Lavrié, J. V.: High-resolution simulations of atmospheric CO_2 over complex terrain – representing the Ochsenkopf mountain tall tower, Atmos. Chem. Phys., 11, 7445–7464, doi:10.5194/acp-11-7445-2011, 2011.

Rayner, P. J., Scholze, M., Knorr, W., Kaminski, T., Giering, R., and Widmann, H.: Two decades of terrestrial carbon fluxes from a carbon cycle data assimilation system (CCDAS), Global Biogeochemical Cycles, 19, GB2026, doi:10.1029/2004GB002254, 2005.

Scholze, M., Kaminski, T., Knorr, W., Voßbeck, M., Wu, M., Ferrazzoli, P., Kerr, Y., Mialon, A., Richaume, P., Rodríguez-Fernández, N., Vittucci, C., Wigneron, J. P., Mecklenburg, S., and Drusch, M.: Mean European carbon sink over 2010–2015 estimated by simultaneous assimilation of atmospheric CO_2, soil moisture, and vegetation optical depth, Geophysical Research Letters, 46, 13796–13803, doi:10.1029/2019GL085725, 2019.

Schürmann, G. J., Kaminski, T., Köstler, C., Carvalhais, N., Voßbeck, M., Kattge, J., Giering, R., Rödenbeck, C., Heimann,

https://doi.org/10.5194/egusphere-2025-6272
Preprint. Discussion started: 31 December 2025

M., and Zaehle, S.: Constraining a land-surface model with multiple observations by application of the MPI-Carbon Cycle Data Assimilation System V1.0, Geosci. Model Dev., 9, 2999–3026, doi:10.5194/gmd-9-2999-2016, 2016.

Super, I., Dellaert, S. N. C., Visschedijk, A. J. H., and Denier van der Gon, H. A. C.: Uncertainty analysis of a European high-resolution emission inventory of CO_2 and CO to support inverse modelling and network design, Atmos. Chem. Phys., 20, 1795–1816, doi:10.5194/acp-20-1795-2020, 2020.

Thompson, R. L., Patra, P. K., Chevallier, F., Maksyutov, S., Law, R. M., Ziehn, T., van der Laan-Luijkx, I. T., Peters, W., Ganshin, A., Zhuravlev, R., Maki, T., Nakamura, T., Ishizawa, M., Saeki, T., Machida, T., Poulter, B., Canadell, J. G., and Ciais, P.: Top–down assessment of the Asian carbon budget since the mid-1990s, Nature Communications, 7, 10724, doi:10.1038/ncomms10724, 2016.

Tian, X., Xie, Z., Cai, Z., Liu, Y., Fu, Y., and Zhang, H.: The Chinese carbon cycle data-assimilation system (Tan-Tracker), Chin. Sci. Bull., 59, 1541–1546, doi:10.1007/s11434-014-0238-1, 2014.

Tian, X., Xie, Z., Liu, Y., Cai, Z., Fu, Y., Zhang, H., and Feng, L.: A joint data assimilation system (Tan-Tracker) to simultaneously estimate surface CO_2 fluxes and 3-D atmospheric CO_2 concentrations from observations, Atmos. Chem. Phys., 14, 13281–13293, doi:10.5194/acp-14-13281-2014, 2014.

Tomohiro, O., Shamil, M.: Center for Global Environmental Research, National Institute for Environmental Studies, ODIAC fossil fuel CO_2 emissions dataset (ODIAC2023) [Dataset], doi:10.17595/20170411.001, 2024.

Vermote, E.: MODIS/Terra surface reflectance 8-day L3 global 500m SIN grid V061[Dataset], https://doi.org/10.5067/MODIS/ MOD09A1.061, 2021.

Wang, S. J., Tian, S. S., Cai, Q. N., Wu, H. Q., and Wu, C. X.: Driving factors and carbon transfer of industrial carbon emissions in Guangdong Province under the background of industrial transfer, Geographical Research (In Chinese), 40(9), 2606–2622, doi:10.11821/dlyj020200916, 2021.

Wang, Y., Huang, C., Hu, X.-M., Wei, C., An, J., Yan, R., Liao, W., Tian, J., Wang, H., Duan, Y., Liu, Q., Wang, W., Ma, Q., He, Q., Cheng, T., Su, H., and Zhang, R.: Quantifying the Impact of COVID-19 Pandemic on the Spatiotemporal Changes of CO_2 Concentrations in the Yangtze River Delta, China, J. Geophys. Res. Atmos., 128, doi:10.1029/2023jd038512, 2023.

Wu, L., Broquet, G., Ciais, P., Bellassen, V., Vogel, F., Chevallier, F., Xueref-Remy, I., and Wang, Y.: What would dense atmospheric observation networks bring to the quantification of city CO_2 emissions?, Atmospheric Chemistry and Physics, 16, 7743–7771, doi:10.5194/acp-16-7743-2016, 2016.

Xiao, X., Hollinger, D., Aber, J., Goltz, M., Davidson, E. A., Zhang, Q., and Moore III, B.: Satellite-based modeling of gross primary production in an evergreen needleleaf forest, Remote Sens. Environ., 89, 519–534, doi:10.1016/j.rse.2003.11.008, 2004a.

https://doi.org/10.5194/egusphere-2025-6272
Preprint. Discussion started: 31 December 2025

Xiao, X. M., Zhang, Q. Y., Braswell, B., Urbanski, S., Boles, S., Wofsy, S., Berrien, M. III, and Ojima, D.: Modeling gross primary production of temperate deciduous broadleaf forest using satellite images and climate data, Remote Sens. Environ., 91, 256–270, doi:10.1016/j.rse.2004.03.010, 2004b.

Xu, R., Tong, D., Xiao, Q., Qin, X., Chen, C., Yan, L., Cheng, J., Cui, C., Hu, H., Liu, W., Yan, X., Wang, H., Liu, X., Geng, G., Lei, Y., Guan, D., He, K., and Zhang, Q.: MEIC-global-CO2: A new global CO_2 emission inventory with highly-resolved source category and sub-country information, Sci. China Earth Sci., 66, doi: 10.1007/s11430-023-1230-3, 2023.

Zhang, H. F., Chen, B. Z., van der Laan-Luijkx, I. T., Chen, J., Xu, G., Yan, J. W., Zhou, L. X., Fukuyama, Y., Tans, P. P., and Peters, W.: Net terrestrial CO_2 exchange over China during 2001–2010 estimated with an ensemble data assimilation system for atmospheric CO_2, Journal of Geophysical Research: Atmospheres, 119, 3500–3515, doi:10.1002/2013JD021297, 2014a.

Zhang, H. F., Chen, B. Z., van der Laan-Luijkx, I. T., Machida, T., Matsueda, H., Sawa, Y., Fukuyama, Y., Labuschagne, C., Langenfelds, R., van der Schoot, M., Xu, G., Yan, J. W., Zhou, L. X., Tans, P. P., and Peters, W.: Estimating Asian terrestrial carbon fluxes from CONTRAIL aircraft and surface CO_2 observations for the period 2006 to 2010, Atmospheric Chemistry and Physics, 14, 5807–5824, doi:10.5194/acp-14-5807-2014, 2014b.